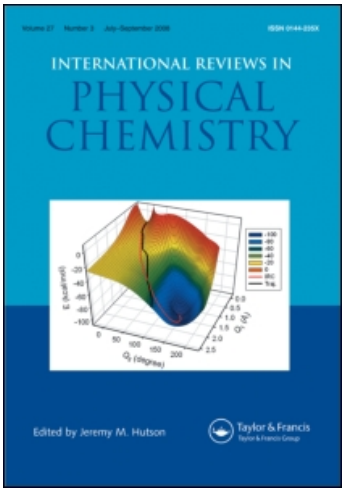

International Reviews in Physical Chemistry
Publication details, including instructions for authors and subscription information:
http://www.informaworld.com/smpp/title~content=t713724383

Spectroscopic studies of the size and composition of single aerosol droplets

Jonathan P. Reid[a]; Helena Meresman[a]; Laura Mitchem[a]; Rachel Symes[a]
[a] School of Chemistry, University of Bristol, Bristol, BS8 1TS, UK

To cite this Article Reid, Jonathan P. , Meresman, Helena , Mitchem, Laura and Symes, Rachel(2007) 'Spectroscopic studies of the size and composition of single aerosol droplets', International Reviews in Physical Chemistry, 26: 1, 139 — 192
To link to this Article: DOI: 10.1080/01442350601081899
URL: http://dx.doi.org/10.1080/01442350601081899

International Reviews in Physical Chemistry,
Vol. 26, No. 1, January–March 2007, 139–192

Taylor & Francis
Taylor & Francis Group

Spectroscopic studies of the size and composition of single aerosol droplets

JONATHAN P. REID*, HELENA MERESMAN, LAURA MITCHEM and RACHEL SYMES†

School of Chemistry, University of Bristol, Bristol, BS8 1TS, UK

(*Received 29 August 2006; in final form 24 October 2006*)

The characterization of aerosol properties and processes, non-intrusively and directly, poses a severe analytical challenge. In order to understand the role of aerosols in often complex environments, it is necessary to probe the particles *in situ* and without perturbation. Sampling followed by end-of-line analysis can lead to perturbations in particle composition, morphology and size, particularly when analysing liquid aerosol droplets containing volatile components. Optical spectroscopy can provide a strategy for the direct assessment of particle size, composition and phase. We review here the application of linear and non-linear Raman spectroscopies in the characterization of liquid aerosol droplets. Spontaneous Raman scattering can allow the unambiguous identification of chemical components and the determination of droplet composition. Stimulated Raman spectroscopy can allow the determination of droplet size with nanometre accuracy and can allow the characterization of near-surface composition. When combined, the mixing state and homogeneity in droplet composition can be investigated. We highlight some applications of these spectroscopic techniques in studies of the kinetics of particle transformation, the equilibrium composition of aqueous aerosol droplets, and the coagulation and mixing state of organic and aqueous aerosol components. Specifically, we examine the heat and mass transfer accompanying the evaporation of volatile components from liquid droplets, the equilibrium size of aqueous/sodium chloride droplets with varying relative humidity, and the mixing of the immiscible decane and water components during droplet coagulation. We conclude by considering the potential of these techniques for improving our understanding of aerosol properties and processes.

Contents

*Corresponding author. Email: j.p.reid@bristol.ac.uk
†Current Address: Actica Consulting Limited, 30 Alan Turing Road, Surrey Research Park, Guildford, Surrey, GU2 7YF, Tel: 01483 540200, Fax: 01483 540201.

International Reviews in Physical Chemistry
ISSN 0144–235X print/ISSN 1366–591X online © 2007 Taylor & Francis
http://www.tandf.co.uk/journals
DOI: 10.1080/01442350601081899

1. Introduction

Aerosols play an important role in a wide range of scientific disciplines including atmospheric chemistry and physics, combustion science, drug delivery and plasma physics. Defined as a dispersion of solid particles or liquid droplets within a gaseous phase, it is crucial that both the condensed phase and the gas phase are characterized if the role of the aerosol is to be fully interpreted. While characterizing the gas phase composition can be accomplished *in situ* by standard techniques, including optical spectroscopy, mass spectrometry and chromatographic techniques, characterizing the condensed phase directly is more challenging [1–7]. Although off-line techniques can be used as an end-of-line analysis following sampling by impactors and filters, it is widely recognized that these can perturb the sample, particularly through the loss of volatile components from the condensed phase [7, 8].

Techniques that probe the condensed phase *in situ* or with minimum perturbation at the sampling stage are essential if the dynamic nature of aerosols is to be fully explored. This provides a significant challenge to analytical science; typical aerosol particles a few microns in diameter correspond to a sample volume on the order of picolitres. Thus, average properties of ensembles are commonly measured. For example, the distribution of particles sizes can be recorded through either optical interrogation or mobility analysis [2, 6]. The average composition of a particle ensemble can be recorded with optical spectroscopy or mass spectrometry [1, 9]. Indeed, it is now possible to interrogate the composition of a single particle with an aerosol time-of-flight mass spectrometer, allowing an examination of the variation in aerosol composition from particle to particle. Optical spectroscopy can provide a non-intrusive alternative for characterizing directly a single particle. In this article we provide a review of the range of observables that can be measured by optical spectroscopy and illustrate the measurement of these observables in a range of applications.

It is instructive to first consider the complexity of the analytical problem. We have already defined an aerosol as a dispersion of solid particles or liquid droplets within the gas phase. Thus, it is important to be able to determine the phase of the particle under examination. A single aerosol particle may be mixed phase, containing different crystalline forms of different components, it may consist of a solid inclusion within a liquid host droplet, or it may contain immiscible liquid phases [1, 10, 11]. In these examples, the different phase components are described as undergoing internal mixing. Alternatively, different phase components may exist as individual particles and are then described as an external mixture.

The phase of the aerosol is determined by the surrounding environment and the history of the particle, as well as chemical composition [10–12]. For a typical inorganic salt at low relative humidities (RHs), the particle exists in a crystalline form. At a RH referred to as the deliquescence point, the crystalline solid particle absorbs water and the inorganic salt dissolves, with the particle undergoing a phase transition from a solid to a liquid, as illustrated in figure 1 [11, 12]. Above this RH, the particle continues to absorb water, growing in size and mass, and the salt becomes more dilute. The activity of the water vapour is equal to the activity of the condensed water at all times and equilibrium is maintained.

If the cycle is reversed and the RH is lowered, the droplet evaporates losing water as the volatile component. However, once it returns to the deliquescence RH it remains in a supersaturated liquid state showing a hysteris in its composition and size until it reaches the efflorescence (or crystallization) RH [11, 12]. In the supersaturated state, it is instructive to consider the concentration of free water and solvated water molecules,

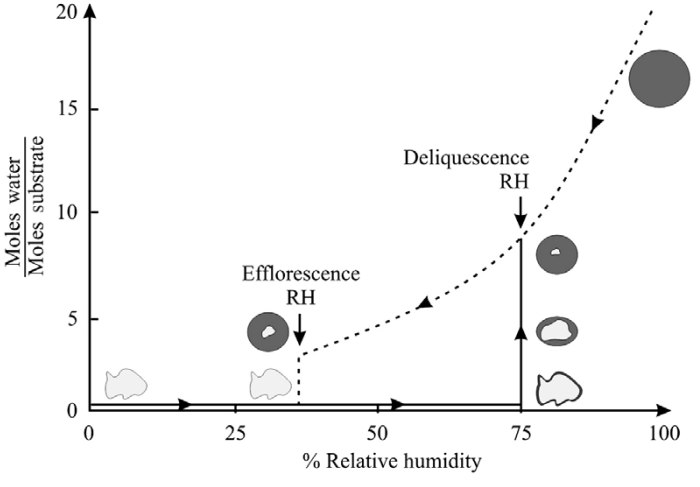

Figure 1. An illustration of the deliquescence/efflorescence cycle for an involatile inorganic solute. At the deliquescence RH, the solid salt particle dissolves, taking up water vapour and forming a dilute aqueous solution droplet (solid line). With increasing RH, the particle continues to increase in size and the aqueous salt solution becomes more dilute. With decrease in RH, the aqueous salt solution becomes supersaturated in the solute, remaining liquid to RHs lower than the deliquescence point (dashed line). Crystallization to form a solid particle occurs at the efflorescence RH. [Figure 1, *Chemical Society Reviews* **32** (2003) 70 – Reproduced by permission of The Royal Society of Chemistry]

which refer to the water molecules interacting with other water molecules and with solute molecules, respectively [13]. It has been suggested that a supersaturated solution does not crystallize until the amount of free water decreases below the amount of solvated water. At this point, the particle undergoes a phase transition, once again becoming a solid particle composed of the inorganic salt. Some residual water may be incorporated within the particle and it may not be completely dry [14, 15]. It is clear that at RHs between the deliquescence and efflorescence points, the phase of the particle is dependent on the recent RH history experienced by the particle.

The presence of an organic component in the aerosol particle can also influence the RHs at which deliquescence and crystallization occur [12, 16, 17]. For example, a mixed ammonium sulphate/glutaric acid particle shows a decrease in the deliquescence RH when compared to an ammonium sulphate aerosol [18–20]. Thus, determining the composition is important if the properties and behaviour of the particle are to be rationalized and the distribution of particle sizes under equilibrium conditions is to be understood.

The presence of a surface active component, a surfactant, within the particle leads to inhomogeneities in composition [17, 21]. With varying droplet size and surfactant concentration, the surface excess of the surfactant will change according to the Gibbs adsorption isotherm. Thus, the surface composition may not reflect the bulk composition of the particle and it may be significantly different. For example, it has been proposed that aqueous atmospheric aerosol containing an organic component such as a long chain fatty acid could adopt a structure analogous to that of an inverse micelle in a microemulsion [21, 22]. The surface active organic component is expected to form a surface layer that appears hydrophobic to a water molecule approaching from the gas phase, altering the affinity of the particle to water and changing its hygroscopicity. Thus, it has been suggested that to some degree the properties of the aerosol and the rate at which the particle can change in size by taking up water vapour are dependent on the composition of the particle surface, as well as the bulk composition [23].

The enriched surface composition of an organic component arising from surfactant behaviour within an aqueous aerosol is but one illustration of the inhomogeneity in composition that may be observed within a particle. Further inhomogeneities may occur during the transformation of a particle. For a multicomponent droplet undergoing rapid evaporation, such as is observed in combustion or in the delivery of pharmaceuticals to the lungs, not only does the composition of the particle change with time if the components have different volatilities, but concentration gradients can exist within the evaporating droplet [24–26]. Different components have different vapour pressures and different diffusion constants, and the rapid depletion of a component near the surface will lead to the rapid development of concentration gradients within the particle on sub-millisecond timescales.

Rapid changes in composition through evaporation or condensational growth can lead to significant changes in particle temperature, dependent on the relative rate of mass transfer and the rate of heat conduction within the particle and between the particle and the gas phase [24, 27–29]. A change in temperature of the particle will lead to ensuing changes in mass flux between the particle and the surrounding gas phase, and an unsteady process of particle evaporation or growth.

To explore the thermodynamic properties of a particle and the kinetics of particle transformation, we can now identify the observables which must be measured. In addition to characterizing the surrounding gas phase composition and temperature, we would ideally characterize the size, composition, phase, refractive index and temperature of a particle. Further, inhomogenieties in composition and temperature can influence mass and heat transfer across the interface between the particle and the surrounding gas phase. Examining gradients in composition and temperature would provide invaluable insights into the processes occurring internally within a particle. The mixing state of different phase components can lead to complex heterogeneity within a particle, even leading to the phase segregation of immiscible liquid components or the inclusion of a solid particle within a liquid host. The coexistence of different phases within a single particle can lead to significant changes in its thermodynamic properties and kinetics of transformation. Thus, techniques must ideally provide a signature of mixing state and phase for the different components.

A range of optical techniques has been used to characterize aerosol particles [24]. By recording the elastic light diffraction pattern, the size and shape of a single particle can be determined [30–34]. Elastic light scattering techniques are usually limited to particles greater than 100 nm in size. For spherical particles smaller than 2 μm in diameter, the scattered light intensity can be used to estimate the size of the particle. At sizes greater than this within the Mie scattering regime [35], the diffraction pattern provides a unique signature of particle size, provided the refractive index is known. Non-spherical particles lead to highly complex diffraction patterns, and the rapid acquisition of a diffraction pattern during the sampling of particles within a gas flow can allow the determination of many particle shapes and morphologies at a high rate [31].

Raman scattering can provide a fingerprint of the composition, size, temperature and phase of a single particle, as well as yielding information on inhomogeneities in composition and refractive index, and on the existence of inclusions in liquid droplets [24, 36–40]. Spontaneous Raman scattering provides a characteristic spectroscopic fingerprint of intramolecular vibrational frequencies that can be used to identify molecular species in a sample and determine composition [36, 38]. Further, Raman line shapes can be used to interrogate intermolecular interactions in the condensed phase [41, 42]. For example, Raman spectroscopy has been used extensively over many decades to investigate the intermolecular interactions and hydrogen bonding that occur in liquid water and ice, and in aqueous solutions of electrolytes with variation in temperature and composition [43–50].

Stimulated Raman scattering (SRS) can provide a sensitive probe of changing droplet composition near the droplet surface [51, 52] as well as providing a unique fingerprint of droplet size for droplets in the Mie scattering size regime [24, 38, 39, 53, 54]. Mie theory predicts a non-uniform distribution of light intensity within a particle, yielding a spectroscopic signature that cannot be assumed to provide an equally weighted signature from all parts of the particle [38]. The occurrence of non-linear processes in microdroplets is in part made possible by this non-uniform intensity of radiation within the particle. In an extreme case, inelastically scattered light may originate solely from the near-surface region of the droplet, from the volume occupied by whispering gallery modes (WGMs), also referred to as morphology dependent resonances or cavity modes [53, 55]. At wavelengths commensurate with WGMs, the light can form a standing wave

circulating near the droplet surface. The light can be considered to undergo total internal reflection each time it approaches the interface, and can remain trapped in a WGM for timescales of nanoseconds. Thus, WGMs provide a mechanism for optical feedback leading to the amplification of Raman scattering and the generation of SRS, also referred to as cavity enhanced Raman scattering (CERS) [56, 57]. The discrete wavelengths at which WGMs appear in the spectrum of SRS are dependent upon the particle size parameter, x:

$$x = \frac{2\pi a}{\lambda} \tag{1}$$

where a is the particle radius and λ is the wavelength of the radiation. This dependence provides access to information about the particle size (through a) [54, 57, 58].

In addition, laser induced fluorescence (LIF) techniques can be used to probe the particle. The distribution of solvated and free water molecules can be interrogated with a fluorescence probe that is sensitive to changes in hydrogen bonding and solvation, providing a direct signature of efflorescence which allows the mechanism of crystallization to be explored [13, 59]. Fluorescence chromophores sensitive to pH, such as the dye acridine, can be used to determine directly the pH of a droplet [60]. Further, a dye with a temperature dependent fluorescence bandwidth can allow the temperature of the droplet to be interrogated [26, 29].

We will review the application of optical techniques in characterizing aerosol particles, concentrating in particular on spontaneous and stimulated Raman scattering and laser induced fluorescence. We will base the discussion largely on our recent work; a broader ranging discussion of the application of optical techniques can be found in references 39 and 40. The focus of this review is on characterizing liquid droplets.

2. Experimental strategies

The experiments that will be reviewed all seek to characterize a single liquid aerosol droplet and determine the ensemble properties from the analysis of many particles. Measurements have been undertaken with droplets spanning the diameter range 1–120 μm using linear and non-linear spectroscopy. Droplets have been probed either while falling in a droplet train apparatus on timescales of milliseconds or while immobilized in an optical trap over timescales of seconds to days. Both pulsed laser and continuous wave (CW) laser techniques have been used to characterize the aerosol droplets. We will now describe the experimental strategies in detail.

2.1. *CW laser and pulsed laser measurements on falling droplets*

A schematic of the experimental design is shown in figure 2. In these measurements, a vibrating orifice aerosol generator (VOAG) is used to generate droplets 10–60 μm in radius. The VOAG operates by forcing liquid under pressure through a small orifice, 10–50 μm in diameter, forming a liquid jet [61]. The instability of the jet to vibration is exploited by applying a regular mechanical disturbance to the jet by modulating the

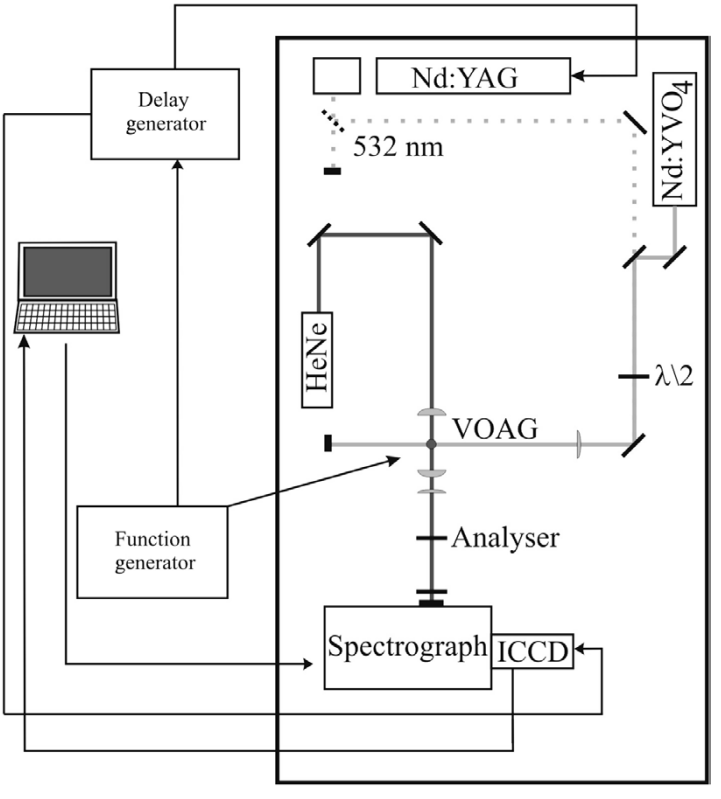

Figure 2. Experimental diagram of the laser Raman spectroscopy measurements performed on a falling droplet train generated by a vibrating orifice aerosol generator (VOAG). The excitation sources include a pulsed Nd:YAG laser operating at 532 nm or 355 nm, or a CW Nd:YVO_4 laser operating at 532 nm. The polarization of the incident laser can be controlled with a half-wave plate ($\lambda/2$) and the polarization of the scattered Raman light can be selected with an analyser. A HeNe laser is used to align the droplet train axis to the optical collection axis. In the pulsed laser experiments, the laser pulse, droplet generation and spectroscopic collection are synchronized with a function generator and digital delay generator.

thickness of a piezoelectric crystal positioned at the generation point of the jet. Thus, the liquid jet is broken-up in a controlled fashion into droplets with a size determined by the orifice diameter, the liquid feed rate and the modulation frequency of the piezoelectric crystal.

The train of droplets is illuminated with the probe laser at a distance of between 1 and 2 cm downstream from the orifice. In the CW laser experiments, the illumination source is a Nd:YVO_4 laser (Coherent VERDI V-5) operating at 532 nm with powers between 100 mW and 5 W. The polarization of the beam is controlled using a zero-order $\lambda/2$ waveplate. Light scattered from the droplets is collected at 90° to the incident direction in the horizontal plane, and focused onto the entrance slit of a spectrograph with a 500 mm focal length, first passing through a long pass filter and a polarization analyser. The spectrograph is equipped with a triple grating turret housing 300 g/mm, 600 g/mm and 2400 g/mm blazed gratings. Dispersed light is detected on an intensified CCD array (1024×256 pixels ICCD, Pi-Max Roper Scientific), and recorded on a PC.

In the pulsed laser measurements, the laser pulse, ~10 ns in duration, is provided by a frequency doubled or tripled Nd:YAG laser (Continuum Surelite) operating at 532 nm or 355 nm, respectively, and at a repetition rate of 10 Hz, allowing 10 droplets to be sampled in one second. The droplet generation and laser pulse are synchronized through a digital delay generator, allowing reproducible alignment of the laser pulse to successive droplets. The laser pulse is typically focussed to a waist comparable in size to the droplet, ensuring that a single droplet is illuminated face on. The time gating on the ICCD is used to collect light during only a narrow time interval following the laser pulse. The remainder of the experimental design is identical to that described previously.

2.2. *CW laser measurements on optically trapped droplets*

We have described the experimental approach for trapping and manipulating aerosol droplets 2–14 μm in diameter with optical tweezers in detail in previous publications [62, 63]. The optical trap is formed by focussing light from an argon–ion laser operating at 514.5 nm, or a Nd:YVO_4 laser (Coherent VERDI V-5) operating at 532 nm, through a microscope objective to form a single-beam gradient force optical trap (optical tweezers). The focused light passes from the objective through an index matching fluid and through a coverslip into an aerosol cell. A dense flow of liquid aerosol droplets is introduced into the cell, produced from a medical nebulizer, and a single droplet is caught from the flow in the optical trap.

As with conventional optical tweezers, in which microscopic objects are immobilized and manipulated in the condensed phase, aerosol tweezers allow the direct control of single or multiple aerosol particles [64, 65]. Although light scattering from a particle exerts a destabilizing force, acting to push the particle along the axis of propagation of the laser beam and out of the most intense part of the beam, a gradient force is exerted on a trapped particle when the light is tightly focussed through a high numerical aperture objective. The refraction of light through a non-absorbing transparent particle leads to a gradient force that acts to pull the particle into the most intense region of the laser beam, as illustrated in figure 3. When the gradient force dominates the scattering force, the particle is immobilized close to the laser focus, and a three-dimensional trap is formed. Trapping efficiencies have been measured that are comparable to the trapping efficiencies reported in liquids, and laser powers as low as 1 mW are required to retain a droplet once trapped [62, 66].

Aerosol tweezing measurements have been performed on two different instruments [63]. The first instrument is based around a commercial Leica DM IRB microscope and the argon–ion laser source. The trapping beam passes through two sets of beam expansion optics, is reflected from a notch filter, then from a dichroic mirror onto the back aperture of the microscope objective. Raman backscattered light from the trapped particle is collimated by the objective, passes through the notch filter and is imaged onto the entrance slit of a 0.5 m spectrograph coupled with a CCD for recording a dispersed Raman spectrum. The polarization of the scattered light reaching the spectrograph is selected with a polarizer and the trapped droplet is imaged using conventional brightfield microscopy.

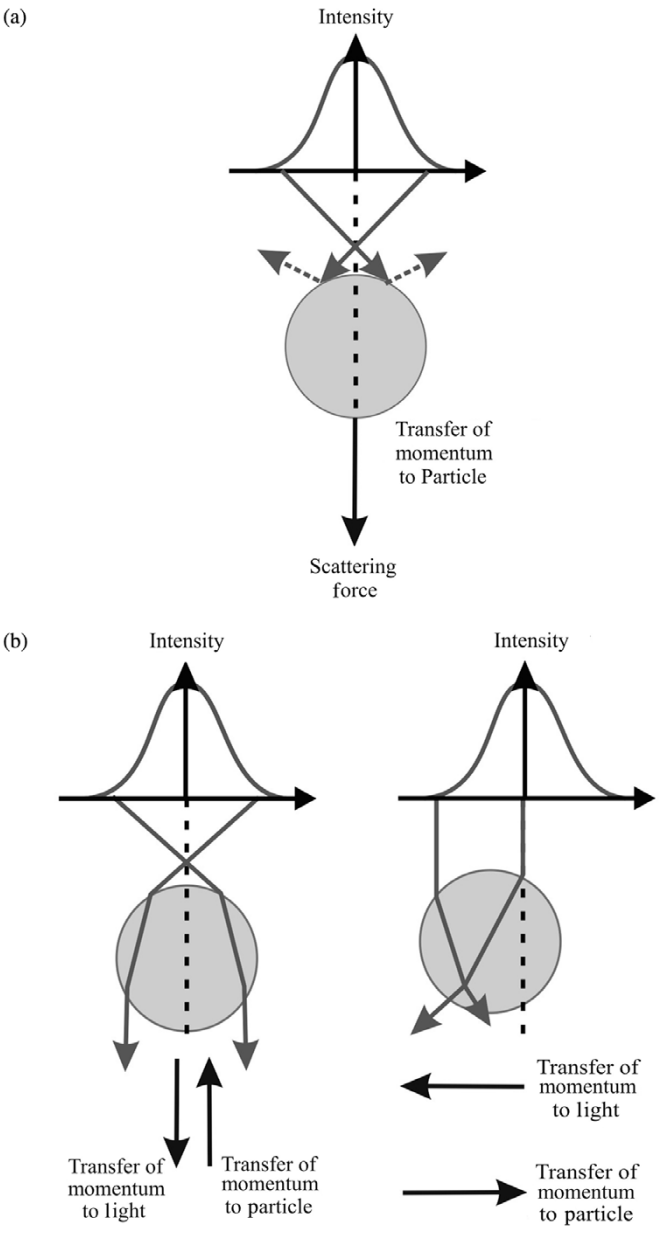

Figure 3. (a) Scattering of photons from a particle leads to a scattering force in the direction of propagation of the light. (b) With a tightly focussed laser beam, a particle sitting below a laser focus or to one side will be drawn into the intense part of the irradiating field by the gradient force.

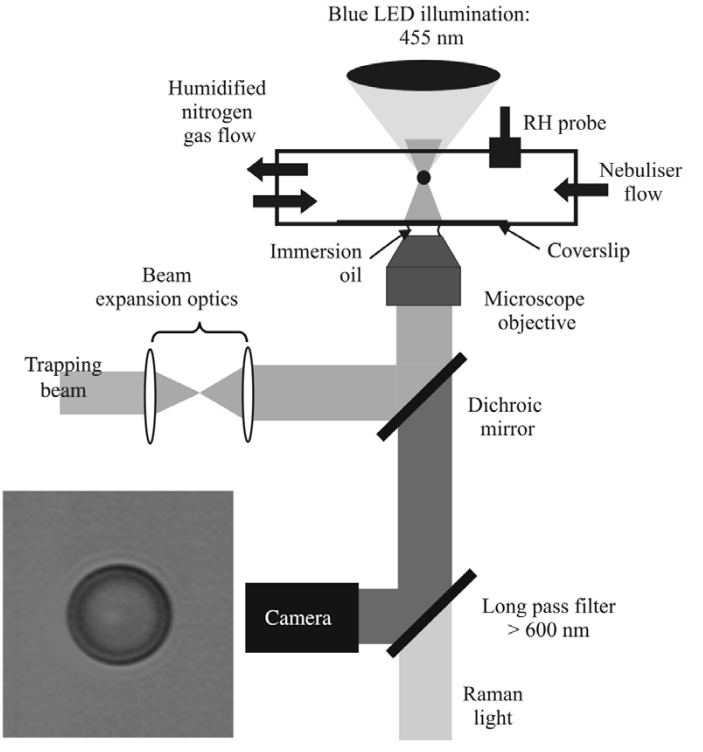

Figure 4. Experimental schematic of the aerosol tweezers instrument. The 532 nm trapping laser beam enters through beam expansion optics and is reflected from a dichroic mirror onto the back aperture of a microscope objective. A single particle is trapped from an aerosol flow within the cell. The composition of the gas phase can be controlled and the RH monitored within the cell. Blue light from an LED operating at 455 nm is used to illuminate the trapped particle to record a conventional brightfield image on a camera. Backscattered Raman light is passed to a spectrograph and CCD to record a spectral fingerprint with a time-resolution of ~1 s. [Reprinted with permission from ref. 63. Copyright 2006 American Chemical Society]

The second instrument is based around a simpler design, not involving the use of a commercial microscope, and using the 532 nm Nd:YVO_4 laser source. A schematic of the instrument is shown in figure 4. Light passes through one set of beam expansion optics, reflects off a dichroic mirror onto the back aperture of the microscope objective. The cone angle of the focussed light, and thus the trapping efficiency, is dependent on the positions of the beam expansion optics and the degree of overfilling of the back aperture of the objective. Illumination of the sample is achieved with the focussed output from a blue LED. The Raman backscattering from the trapped particle and the illumination light are collected by the objective and pass through the dichroic mirror to a long-pass 600 nm filter inclined at 45°. The short wavelengths in the blue are reflected to a camera for imaging and the long wavelengths are imaged onto the entrance slit of a 0.5 m spectrograph with CCD camera allowing spectra to be acquired with a spectral resolution of 0.05 nm. Typical integration times for collecting Raman spectra are 1 second and droplets can be trapped indefinitely.

3. Spontaneous Raman scattering

With the aim of comparing the linear and non-linear Raman spectroscopy of water droplets, it is first necessary to compare spontaneous Raman scattering from microdroplets with Raman scattering in the bulk phase. The bulk phase spectroscopy of liquid water samples has been discussed extensively in the literature over a period of several decades, primarily due to interest in the rich and often ambiguous structural information which may be obtained [41, 43–50, 67, 68]. The spontaneous Raman spectra of liquid and ice phases are considerably more complex than that of the gas phase. The normal modes of an isolated (i.e. gas phase) water molecule (C_{2v} symmetry) transform as two modes of a_1 symmetry (a symmetric stretch and a bend), and one of b_2 symmetry (asymmetric stretch). The vibrational frequencies of these modes are 3657, 1595 and 3756 cm^{-1} respectively [42].

Spontaneous Raman spectra obtained from a bulk liquid water sample and an aqueous aerosol droplet are presented in figure 5, showing the Stoke's shifted band. Excellent agreement between the spectral band shapes and relative intensities of the bulk phase and droplet measurements are observed. The band visible at 1645 cm^{-1} is assigned as the bending vibration, a very weak combination band (of the 1645 cm^{-1} bending and the 686 cm^{-1} librational mode) is visible at 2125 cm^{-1}, and a broad OH stretching band between ~3000 and 3600 cm^{-1} dominates the spectrum. This has a maximum at 3480 cm^{-1} with a strong shoulder visible at 3290 cm^{-1}.

'Mixture' and 'continuum' models have been suggested to account for the shape of the OH stretching band [44, 67–74]. In the former water is assumed to be composed of a mixture of discrete species and in the latter it is represented by a continuum of states. The shape of the band reflects the perturbation of the OH covalent bond, and hence vibrational frequency, by the existence of intermolecular hydrogen bonds. We shall return to this later.

Spontaneous Raman spectra are sensitive to the polarization of the incident light, the collection geometry and the orientation of the transmission axis of any analyser used in the collection axis [47]. As illustrated in figure 6, illumination in these measurements is with vertically polarized light. Selection of vertically polarized Raman scatter at 90° leads to collection of the parallel component of the scattered light. Selection of the horizontal polarized Raman scatter leads to collection of the depolarized perpendicular scattering component. Spontaneous spectra obtained under unpolarized, parallel and perpendicular geometries ([Z(Y, Y + Z)X], [Z(Y, Y)X] and [Z(Y, Z)X] respectively) from bulk and droplet samples are shown for comparison in figure 5. As described above, the spontaneous Raman band shapes recorded from the bulk phase and droplet measurements are consistent for all polarizations. The low frequency shoulder transforms as the totally symmetric vibration of a_1 symmetry, leading to a parallel scattering component in the Raman fingerprint [43, 45–47]. The high frequency peak transforms as an asymmetric vibration of b_2 symmetry. In this case, the parallel component of the Raman scatter is accompanied by a degree of depolarization [43, 45–47]. This is shown schematically in figure 7. Thus, an examination of the parallel scattering component leads to the appearance of the whole OH stretching band, while

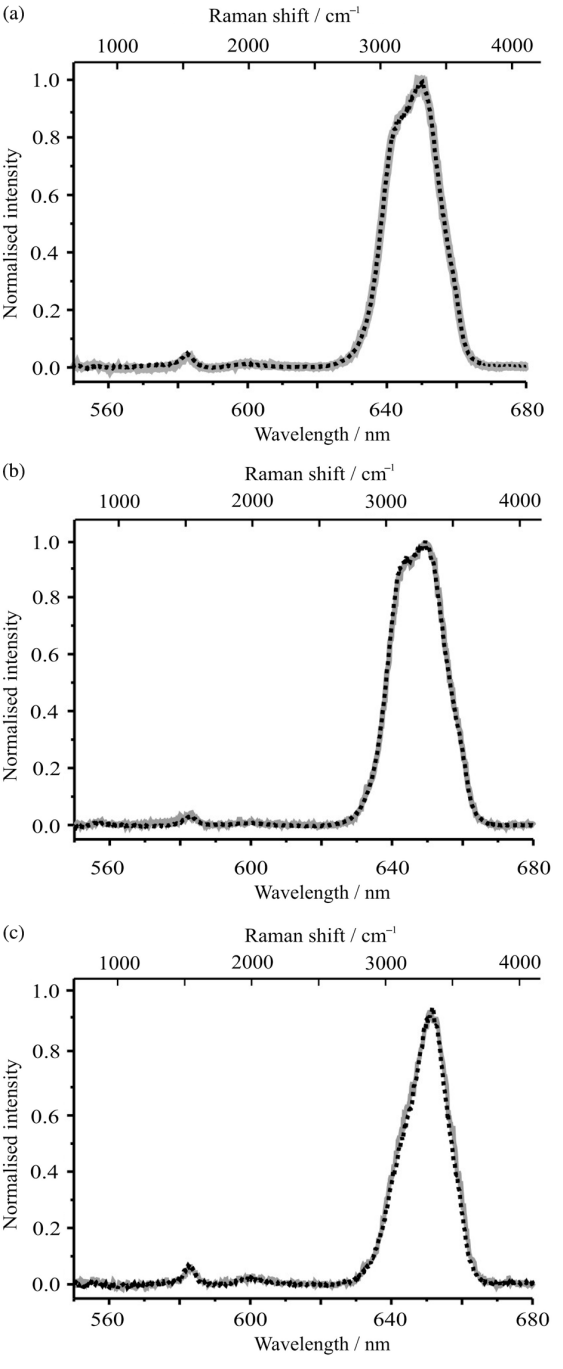

Figure 5. Comparison of the spontaneous Raman spectra from droplets ~38–42 μm in radius (grey thick line) and a bulk phase sample (black dotted line). (a) Illumination with vertically polarized light and unpolarized collection of scatter [Z(Y, Y + Z)X]. (b) Illumination with vertically polarized light and collection of the parallel vertically polarized scatter [Z(Y, Y)X]. (c) Illumination with vertically polarized light and collection of the perpendicular horizontally polarized scatter [Z(Y, Z)X]. All spectra represent 50 s integration.

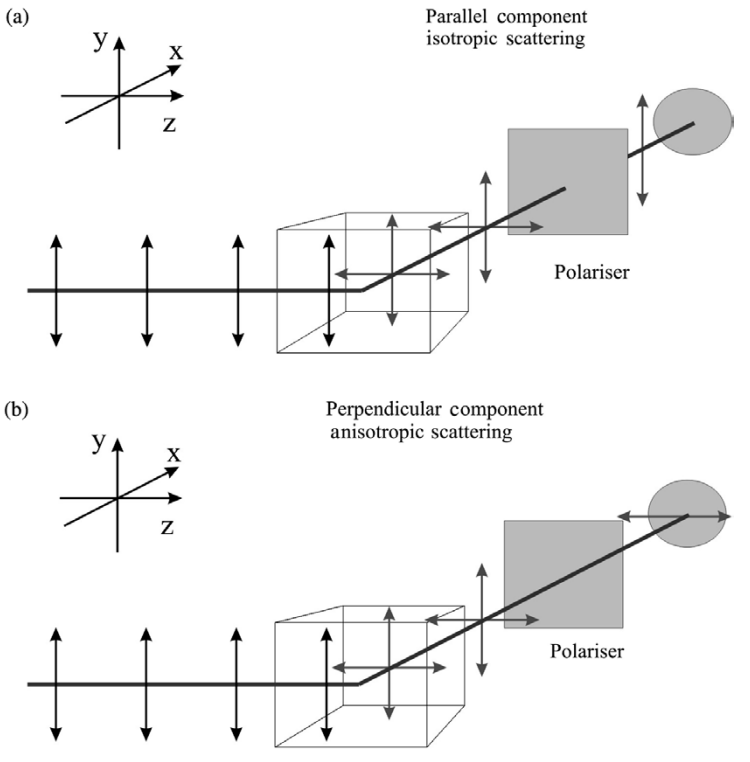

Figure 6. Illustration of the experimental collection scheme for the (a) parallel and (b) perpendicular Raman scattering components.

selection of the perpendicular scattering component leads to the observation of scattering from only the higher Raman shift side of the band that arises from depolarization [47].

A comparison of the absolute intensities of the scatter reaching the detector is shown in figure 8. The depolarization ratio is defined as

$$\rho = \frac{I_{\perp}}{I_{//}} \tag{2}$$

and it is clear from the parallel and perpendicular polarized spectra that the ratio is less than 0.75. This is consistent with a dominant component of the vibrational band arising from a vibration of a_1 symmetry.

The purpose of examining the spontaneous scatter from water droplets and comparing with bulk measurements is to establish whether or not the droplet environment significantly affects the depolarization ratio, and whether the spectra show any features which may be due to surface structure and which are not observed from bulk phase measurements. In each case, the droplet spectrum is consistent with the bulk phase spectrum within the noise of the measurements. Absolute intensities show the expected decrease from unpolarized collection, to parallel collection to

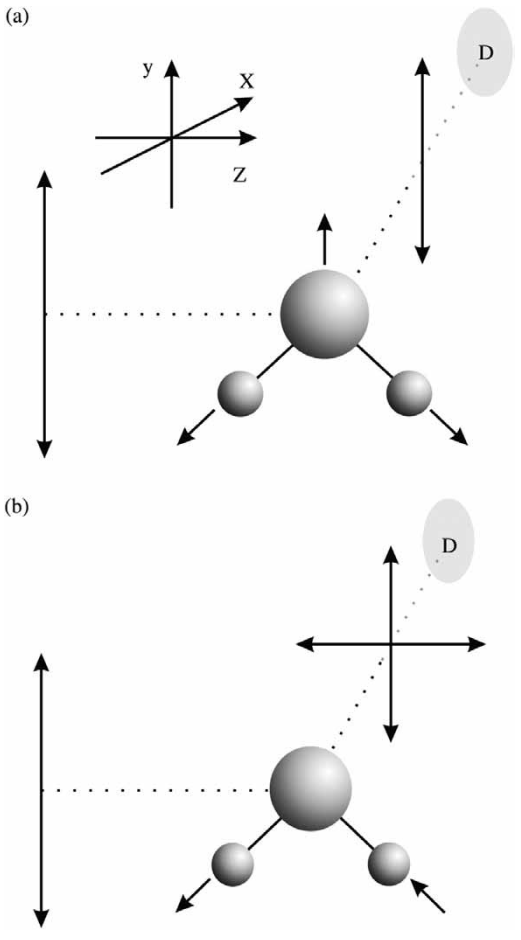

Figure 7. Schematic of the (a) symmetric and (b) asymmetric stretching vibrations of a water molecule and the polarization of scatter observed at the detector (D).

perpendicular collection. These data provide no evidence to suggest that the droplet environment significantly affects the observed depolarization ratios, nor that effects due to surface sampling are discernable. The first result is consistent with the prediction from Mie theory [35] that no depolarization in elastic scattering is expected for scattering from a spherical particle. The second result is consistent with the surface-to-volume ratio for these droplets and the uniformity of illumination arising from approximately plane wave illumination.

Similar studies comparing bulk phase and droplet spontaneous spectra have been made using both single droplet and ensemble measurements [75, 76]. Both these studies found that droplet and bulk samples gave equivalent spectra. The conclusions drawn from these studies were therefore that the spherical boundary of the droplet had no influence on the depolarization ratios observed, and that there was no signature of the surface evident in the data. The results presented above are in complete accordance with the conclusions of these studies.

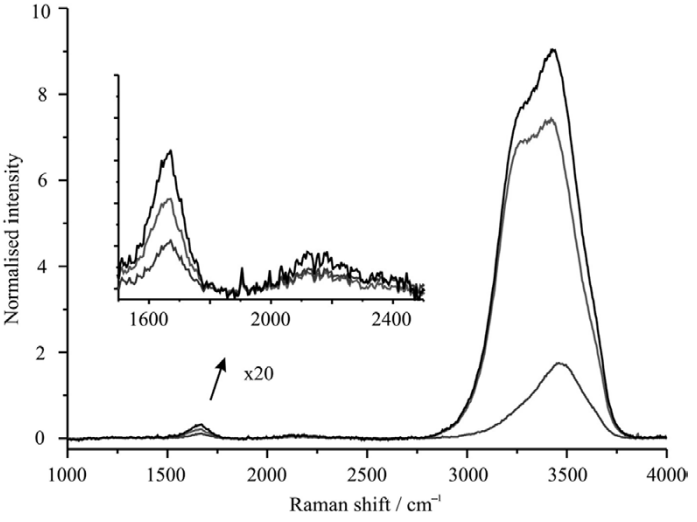

Figure 8. Polarization dependence of the absolute intensities of the OH vibrational bands. The intensity of the unpolarized spectrum is strongest for all bands shown, followed by the intensity recorded from the parallel collection component, and then by the perpendicular collection component.

The shape of the OH stretching band shows a systematic dependence on temperature [43, 44, 46–48] and solute concentration [41, 45, 50]. A change in the hydrogen bonding network in the aqueous phase resulting from a change in temperature or ionic strength leads to a change in the distribution of vibrational frequencies and a change in the band shape. To quantify the change in shape, the vibrational band is commonly deconvoluted into as many as five Gaussian components [50]. The relative weightings of these five components in forming the resulting band shape change with variation in temperature and ionic strength. With increasing temperature, the contribution of the Gaussian components with low Stoke's shift below 3300 cm^{-1} decrease in weighting relative to those at high Stoke's shift. This reflects a weakening of the degree of hydrogen bonding within the liquid phase and a decrease in proportion of strongly hydrogen-bonded water molecules with high coordination. Thus, the low intensity shoulder at 3290 cm^{-1} is observed to decrease in intensity relative to the peak maximum at 3480 cm^{-1} with increasing temperature.

With variation in solute concentration, some inorganic ions are referred to as 'structure making' solutes (such as F^-) and others as 'structure breaking' solutes (such as Cl^-) [50]. The addition of a structure breaking solute such as sodium chloride leads to a reduction in the weighting of the Gaussian components representing the highly coordinated strongly hydrogen-bound water molecules with low Stoke's shift below 3300 cm^{-1}. As with increasing temperature, the low intensity shoulder at 3290 cm^{-1} is observed to decrease in intensity relative to the peak maximum at 3480 cm^{-1} with increasing solute concentration. Thus, the shape of the OH band can be used as an indirect probe of the ionic strength of a droplet for droplets containing Raman inactive solutes such as sodium chloride.

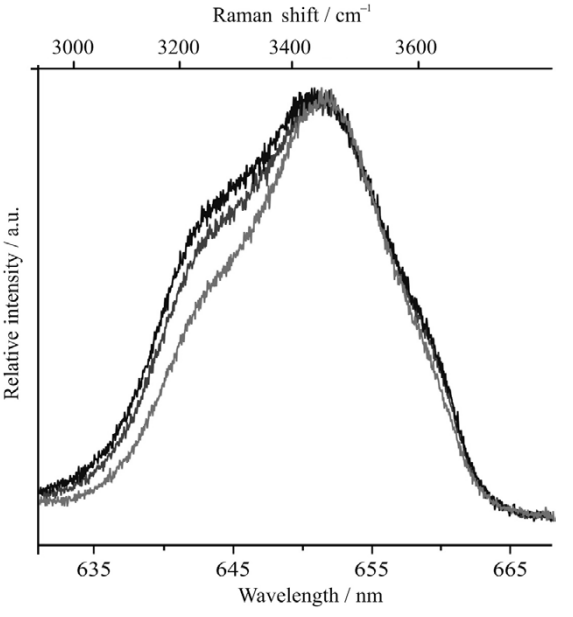

Figure 9. An illustration of the change in the OH stretching Raman band shape with variation in concentration of NaCl, recorded from optically trapped aqueous droplets of composition 0.04, 0.34 and 1.28 M salt (black, dark grey, light grey, respectively). This is recorded with an excitation wavelength of 532 nm.

This behaviour in the OH band shape has been exploited in the characterization of the salt concentration of optically trapped aqueous aerosol droplets containing sodium chloride, as illustrated in figure 9 [63]. The variation in the band shape for three different droplets with different sodium chloride concentrations of 0.04, 0.34 and 1.28 M is clear. With increasing salt concentration the shape of the OH band of the optically trapped droplet is observed to change in the way anticipated, with a decrease in intensity of the low Raman frequency components relative to the high frequency components.

Compositional measurements can be directly performed on aqueous droplets containing a second Raman active component such as nitrate or sulphate anions [77–79]. For these species, the Raman active vibrational modes [80, 81] are listed in table 1 with corresponding spontaneous Raman spectra presented in figures 10(a) and (b). The concentration of the anions can be determined directly by using the intensity of the water OH stretching band as an internal standard, as illustrated for the nitrate ion in figure 11. In this measurement, the symmetric stretching vibration of the anion was used to determine the nitrate concentration. A detection limit of $\sim$2.5 mM has been estimated for the detection of the sulphate and nitrate anions in a 45 μm diameter droplet [79].

4. Stimulated Raman scattering

The thresholds in laser irradiance for non-linear processes such as SRS [56, 82–86], coherent anti-Stokes Raman scattering [87], stimulated Brillouin scattering [88–90],

Table 1. Raman shifted wavelengths and vibrational frequencies for the sulphate and nitrate anions and the water molecule.

Species	Vibration	ν/cm^{-1}	λ/nm (532 nm pump)
$SO^{2-}_{4\,(aq)}$	ν_2	451.5	545.1
$SO^{2-}_{4\,(aq)}$	ν_4	619	550.1
$SO^{2-}_{4\,(aq)}$	ν_1	980.4	561.3
$SO^{2-}_{4\,(aq)}$	ν_3	1107	565.3
H_2O	ν_2	1650	583.2
H_2O	ν_1	3280	644.5
H_2O	ν_3	3490	653.3
$NO^{-}_{3\,(aq)}$	ν_1	1049	563.4
$NO^{-}_{3\,(aq)}$	ν_2	830	556.6
$NO^{-}_{3\,(aq)}$	ν_3	1395	574.6
$NO^{-}_{3\,(aq)}$	ν_4	~723	553.3

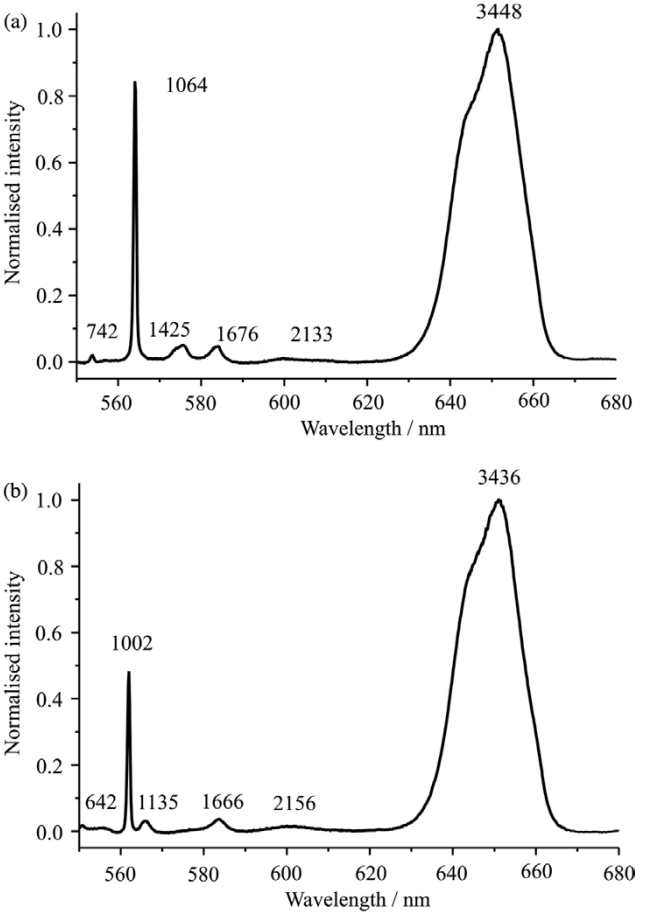

Figure 10. Normalized [Z(Y, Y + Z)X] spontaneous Raman spectra from solutions of (a) 1 M $NaNO_{3\,(aq)}$ and (b) 1 M $Na_2SO_{4\,(aq)}$. Numbers refer to the measured Stoke's shift of each band, in cm^{-1}. This is recorded with an excitation wavelength of 532 nm.

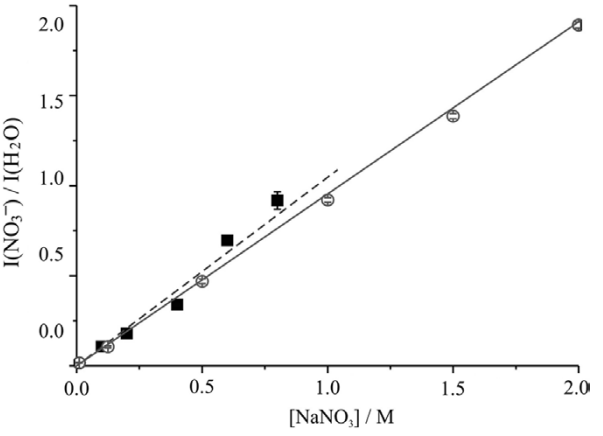

Figure 11. Spontaneous calibration curves for the nitrate ion from bulk (open circles) and droplet (radii ~55 μm, filled black squares) measurements for comparison. The calibration curves were determined from the [Z(Y, Y + Z)X] spontaneous Raman spectra. Linear fits are constrained to the origin (solid grey line – bulk fit, dotted grey line – droplet fit).

lasing [91, 92], and third-harmonic generation [93, 94] are considerably lower in droplets than in bulk phase measurements. The low threshold intensities arise from the ability of the droplet to act as a low loss optical cavity [53, 55, 86, 92]. Cavity quality factors can be in excess of 10^6 for WGMs corresponding to a lifetime of nanoseconds and a pathlength that may be metres within a droplet a few microns in diameter [95, 96]. Thus, WGMs provide a mechanism for optical feedback as illustrated in figure 12 [37]. Incident laser light induces Raman scattering from the molecular constituents of the droplet (figure 12a). At Raman scattered wavelengths commensurate with WGMs, the inelastically scattered light can become trapped within the droplet leading to a buildup of Raman scattered light at these wavelengths (figure 12b). Once a threshold scattering intensity is reached, the round-trip gain in Raman scattered light circulating within the WGMs exceeds the round-trip loss and the Raman scattering intensity grows exponentially as SRS occurs (figure 12c).

In this section, we describe the nature of WGMs in greater detail before examining SRS from water droplets and comparing it to spontaneous scattering. We then describe the application of SRS in the determination of droplet composition, particularly focussing on the importance of the threshold and resonance conditions.

4.1. *Whispering gallery modes*

Whispering gallery modes arise from the formation of a standing wave within a droplet [35, 53, 55]. An example is shown in figure 13. The mode number, n, describes the angular dependence of the WGM and specifies the number of wavelengths forming the standing wave around the droplet circumference, taking only integer values and having a value of 71 in this example. Thus, for light at a resonant wavelength, λ_{res}, the mode number satisfies the following condition:

$$n\frac{\lambda_{res}}{m} < 2\pi a, \tag{3}$$

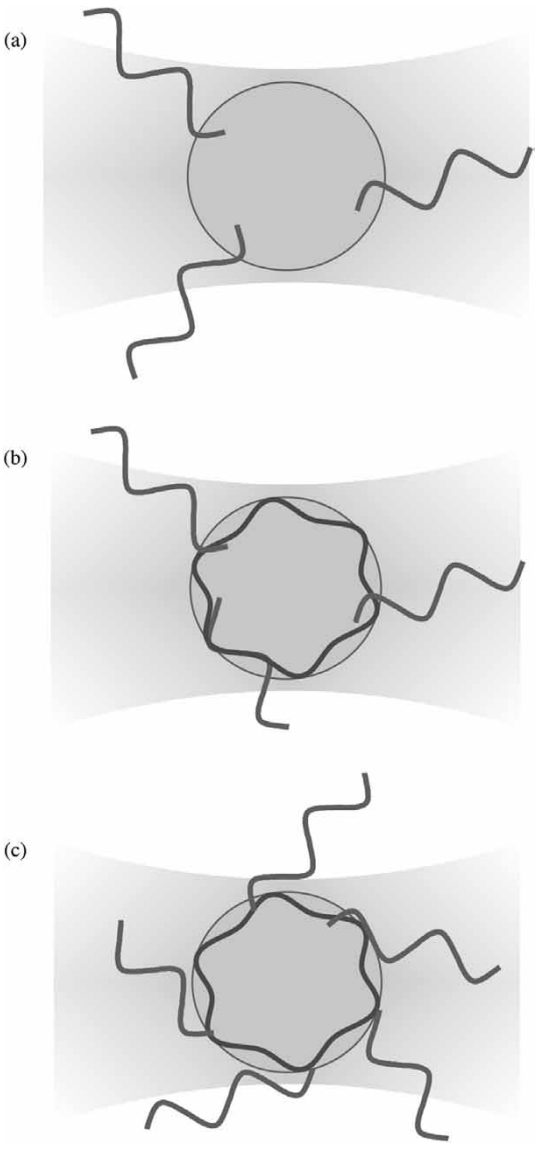

Figure 12. Schematic of SRS generation from droplets: (a) Laser illumination leads to Raman scattering from the droplet constituents; (b) Some wavelengths within the spontaneous Raman scattering spectral band are commensurate with WGMs and can become trapped within the droplet for timescales of nanoseconds; (c) The intensity of the spontaneous Raman scattering circulating in a WGM can exceed a threshold intensity leading to the generation of SRS.

where m is the refractive index of the medium of the particle. This corresponds to the condition that n wavelengths inside the spherical particle must be less than the droplet circumference.

The mode order, l, specifies the radial dependence of the WGM and describes the number of maxima in the mode intensity along the radial coordinate, taking positive

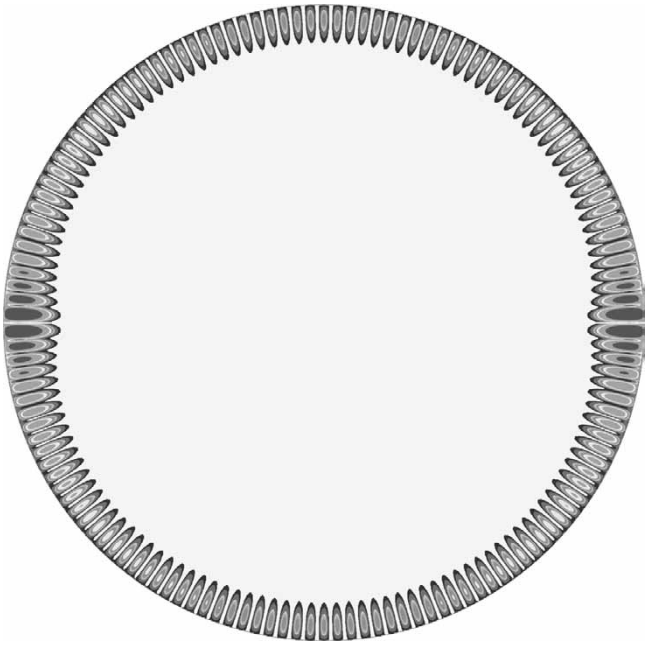

Figure 13. An example of the internal mode intensity for a first-order mode with mode number 71.

integer values of $1, 2, 3, \ldots$ [53, 97]. A comparison of the radial dependence of the mode intensity is shown in figure 14 for modes of order 1, 2 and 7. The maximum intensity of the light within the droplet occurs near the surface, as described above. Further the intensity penetrates to a greater depth with increasing mode order. The penetration depth can be estimated from the ratio a/m [53, 98]. Thus, for a water droplet of refractive index 1.33 and radius 4 μm, the peak intensity occurs at a distance of 3 μm from the droplet centre. Light passing at distances closer to the droplet centre approaches the interface at an angle below the critical angle and does not undergo total internal reflection.

The polarization of the mode must also be specified. Transverse electric (TE) modes show no dependence in the electric field amplitude along the radial coordinate. Transverse magnetic (TM) modes show no dependence in the magnetic field amplitude [55]. In the discussion that follows, all modes are assigned with the notation, TE_n^1 or TM_n^1. All modes also exhibit an azimuthal degeneracy of $(2n+1)$ [53, 55].

Modes of the same polarization and mode order are approximately equally spaced in size parameter [99, 100]. Thus, the WGMs appear as a regular progression of modes in an SRS spectrum, equally spaced in wavelength. The spacing between modes in the large particle limit can be estimated from the equation:

$$\Delta\lambda \sim \frac{\lambda^2}{2\pi a}\frac{\tan^{-1}\rho}{\rho} \quad \text{where } \rho = (m^2 - 1) \tag{4}$$

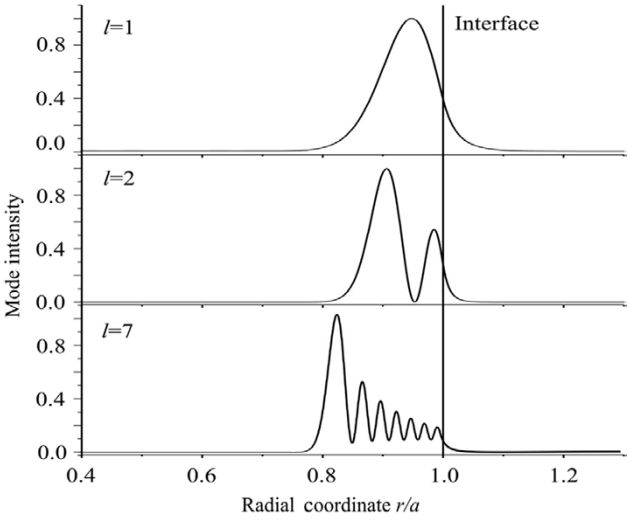

Figure 14. The mode order is defined as the number of maxima in the radial dependence of the mode intensity. Examples are shown of modes with orders of 1, 2, and 7. The concentration of the mode intensity near the interfacial region is apparent.

Further, modes of the same mode number but adjacent mode orders (l and $l+1$) are spaced by [53]

$$\Delta\lambda \sim \frac{\lambda^2}{2\pi a}\frac{\pi}{\rho} \tag{5}$$

for a droplet of radius a.

The lifetime of a WGM is characterized by the quality factor of the resonant mode, Q, reflecting that the particle behaves as a low loss optical cavity of high finesse when on resonance with the wavelength. Q is related to the average lifetime of a photon in a WGM, τ, at the resonant frequency ω_0 [53].

$$Q = \frac{\omega_0}{\Delta\omega} = \omega_0\tau \tag{6}$$

Typical experimentally observed quality factors are of the order of 10^7, equivalent to an average mode lifetime of 20 ns in the visible part of the spectrum [95, 96]. The resonances exhibit a Lorentzian lineshape with a spectral linewidth at full-width half-maximum of $\Delta\omega$. Thus, at a wavelength of 600 nm and for a mode with a quality factor of 10^7, the linewidth will be $0.0017\,\mathrm{cm}^{-1}$. The quality factor is independent of azimuthal mode number due to spherical symmetry, but decreases with increasing mode order [101].

4.2. *Raman spectroscopy of optically trapped aerosol droplets*

The Raman spectra of three aqueous sodium chloride droplets of different sizes acquired while the droplets were held within an optical trap are shown in figure 15 [62].

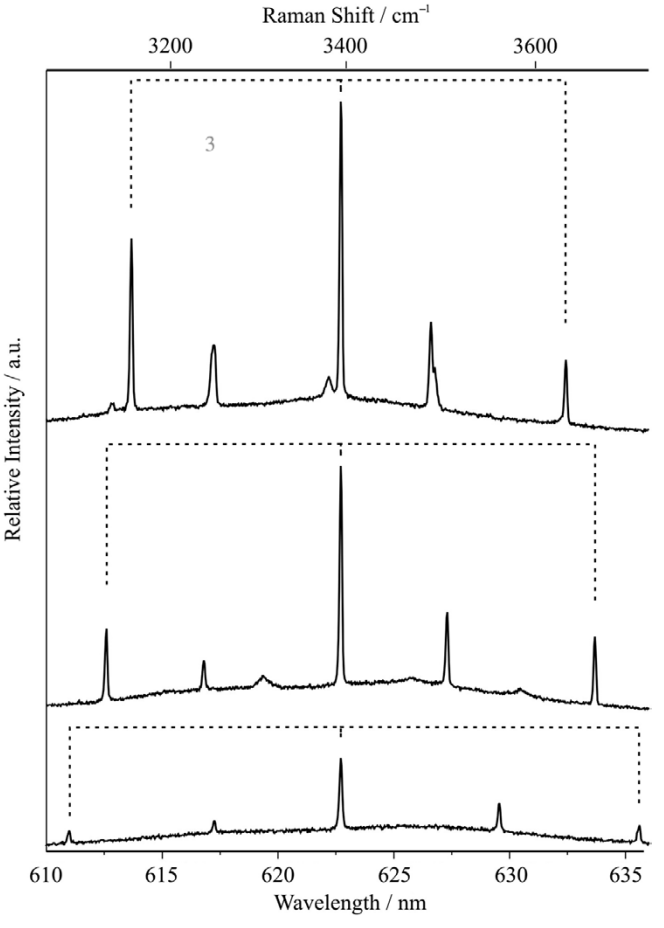

Figure 15. Raman spectra from three droplets of different sizes (5.103, 4.547 and 3.918 μm from top to bottom, respectively). The underlying spontaneous Raman scattering is evident, along with the resonant structure arising from SRS at WGM wavelengths. Pogressions of modes of the same polarization and order are bracketed together by the dashed lines. This is recorded with an excitation wavelength of 514.5 nm. [Ref. 62 – Reproduced by permission of the PCCP Owner Societies]

The underlying spontaneous Raman scattering from the OH stretching vibration of the water within the droplet is clearly visible. This has been described earlier. In addition, resonant structure appears superimposed on the spontaneous Raman band. The structure arises from the enhancement in Raman scattering at wavelengths commensurate with WGMs [63]. As described above, at these wavelengths the spontaneous intensity of Raman scattering surpasses a threshold intensity above which optical feedback leads to the amplification of Raman scattering and the occurrence of SRS. The mechanism will be described in greater detail in a subsequent section. However, at this stage it is instructive to consider the information that can be gained from this structure as it appears in the Raman spectrum.

WGMs occur at discrete values of the size parameter and refractive index. Thus, if the wavelengths of WGMs are measured and the refractive index of the droplet is accurately known, the radius of the droplet can be accurately determined [39, 54, 58, 102]. The accuracy with which the size can be calculated is thus determined by the accuracy associated with the refractive index and the spectral resolution of the wavelength measurement. With the spectral dispersion of $\sim$0.02 nm/pixel common to our measurements, the size of the droplet can be routinely estimated with a precision of $< \pm 2$ nm [63, 103]. The wavelengths of WGMs for a droplet of a first guess radius and refractive index are calculated from Mie scattering calculations. Then, by comparing the calculated wavelengths with the experimental measurements, the size is varied iteratively until the minimum fitting error is achieved. From the best-fit size, the WGMs appearing in the Raman fingerprint can be assigned a mode number, order and polarization.

The assignment of the WGMs appearing in the Raman fingerprint can allow the temporal variation in the droplet size to be interrogated. Resonant modes shifting to the blue indicate that the trapped droplet is evaporating: for a mode of a given number, a shorter wavelength is required to form the standing wave within the droplet as the droplet diminishes in size [39, 63]. Resonant modes shifting to the red indicate that the droplet is growing in size. An example of the variation in spectral fingerprint with time illustrating the change in the wavelength of the WGMs is shown in figure 16. An assignment of the modes is also shown. The variation in droplet size is $\sim$80 nm, and this is clearly discernable from the variation in the Raman fingerprint with time.

Having illustrated the value in recording WGM wavelengths for determining the droplet size with high accuracy, we now turn our attention to address in more detail the origin of the non-linear spectroscopic component of the Raman fingerprint.

4.3. *Pulsed laser SRS spectroscopy of aqueous droplets*

A number of studies have been published which investigate the SRS from bulk water samples. Such experiments were first carried out in the 1970s, with the aim of resolving the debate on the structure of liquid water [104, 105]. Early work was aimed at providing conclusive evidence for the mixture model of water. The exclusive observation of peaks at shifts which corresponded to the peaks of components within the Gaussian decomposition of the spontaneous Raman scattering band was taken as conclusive evidence of the veracity of the mixture model of water. However, these conclusions were refuted in a later paper by Sceats *et al*., in which these features were considered likely to be artefacts due to self-phase modulation caused by pulse distortion, and broadening [106]. More recent work has examined SRS at interfaces, and discrepancies between forwards and backscattered SRS [107, 108].

We describe in this section SRS measurements made on single aqueous droplets using pulsed laser illumination. Compared to the work described in section 3, the much higher irradiances associated with a nanosecond laser pulse than a CW laser lead to the dominance of SRS, rather than spontaneous scattering, in the spectral fingerprint [37, 63]. The measurements reviewed here were carried out in the manner described in section 2 using a droplet train apparatus and pulsed laser illumination.

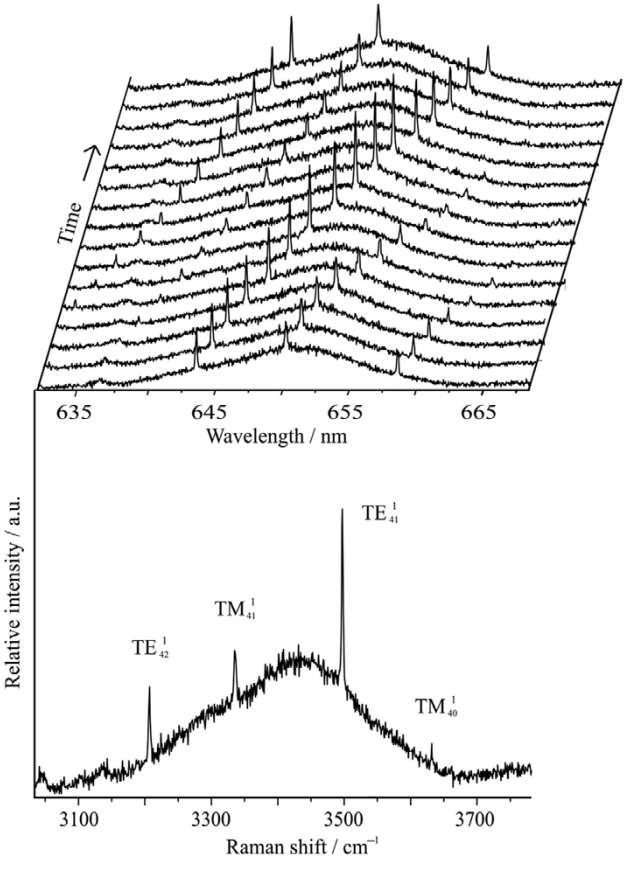

Figure 16. An example of the temporal evolution in droplet spectrum during a period of ~800 s. The droplet increases from a size of 3.49 μm to a size of 3.57 μm over the time frame shown. The growth in the droplet is apparent from the tracking of modes to higher wavelength. The mode assignment is shown. This is recorded with an excitation wavelength of 532 nm.

Single droplet, single pulse SRS spectra vary dramatically in their appearance and intensities, and are strongly dependent on the sampled irradiance and droplet size [109, 110]. Small changes of the particle radius are sufficient to significantly shift the wavelengths of WGMs, such that different wavelengths within the spontaneous Raman envelope are sampled. Variation of the incident intensity leads to a corresponding exponential change in the intensity of the stimulated scatter. In addition, for sequentially probed droplets of different size, the excitation of a different set of resonances with different quality factors leads to variations in the intensity of the SRS.

In order to minimize the effects of the variation in droplet size and alignment and to allow routine interpretation of SRS spectra, a composite spectrum recorded by signal-averaging the output from several hundred droplets is used in the analysis presented in this work [109]. This process has the advantage of averaging such fluctuating properties as the position of the droplet with respect to the interrogation pulse (hence the sampled irradiance) and the quality factors of specific WGMs (hence the circulating intensity).

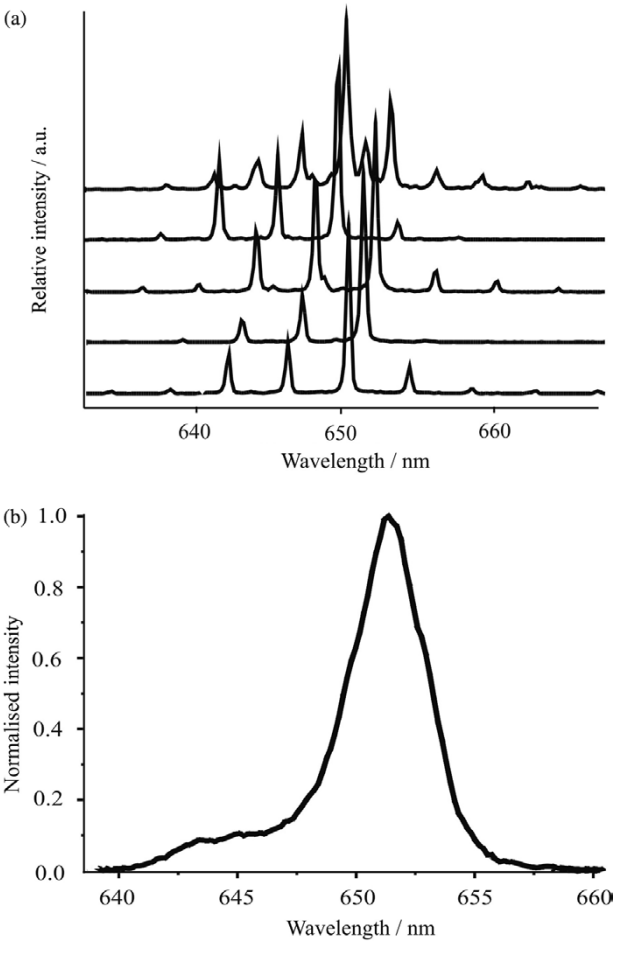

Figure 17. (a) SRS spectra from 5 separate droplets, each with radii ~15 μm and recorded with a single laser pulse. This illustrates the dramatic shift in WGM wavelengths from droplet to droplet due to instability in the droplet generation. (b) A composite spectrum, formed from adding together 500–1000 single droplet spectra. The averaging of the structure is apparent and permits the routine analysis of droplet SRS measurements. This is recorded with an excitation wavelength of 532 nm.

Further, it ensures that the entire spontaneous Raman envelope is sampled by a range of droplet sizes through excitation of a varying set of cavity resonances. This allows the construction of a composite spectrum which is continuous in intensity over the wavelength range of the spectral band. Thus, the composite spectrum may be assumed to represent the average SRS envelope due to all droplets sampled, and should be consistent with spontaneous spectra where competing non-linear effects are absent. An example of this process is shown in figure 17.

The wavelength dependence of the SRS intensity, $I_{SRS}(\lambda)$, is related to the appropriate spontaneous intensity, $I_0(\lambda)$, by the equation [37, 109, 111],

$$I_{SRS}(\lambda) = I_0(\lambda)\exp[(GTI_L\kappa - L)a\Phi] \tag{7}$$

where G is the Raman gain, I_L is the intensity of the pump light within the droplet and κ is the Purcell factor describing the quantum electrodynamic enhancement of the transition rate [112–115]. The spatial overlap of the internal laser field within the droplet and the output resonant WGM leading to SRS signal is given by the overlap integral, T. Thus, $GTI_L\kappa$ describes the growth of intensity at the scattered Raman frequency. The unit length loss of intensity at the same frequency is given by L. The pathlength around the droplet is given by $a\Phi$, where a is the droplet radius and Φ is the angular change on propagation. For stimulated scatter to surpass threshold, it is required that the condition:

$$GTI_L\kappa > L \tag{8}$$

is satisfied. Further, as the gain is proportional to the number density of the scattering species, a threshold number density (or concentration), N_j^{thr}, may be defined at a particular laser light intensity for detection of the species by SRS. The dependence of the threshold number density can be expressed as [116]:

$$N_j^{thr} \propto \frac{L}{\sigma T I_L \kappa} \tag{9}$$

where σ is the Raman cross-section of the scattering species. This threshold level of scatter describes a lower detection limit for the concentration of a species from which SRS may be observed [37, 109].

From equation (7), we calculate the ratio of SRS intensities obtained at two different resonant wavelengths, λ_1 and λ_2, from the expression:

$$\frac{I_{SRS}(\lambda_1)}{I_{SRS}(\lambda_2)} = \frac{I_0(\lambda_1)\exp[(\kappa(\lambda_1)G(\lambda_1)T(\lambda_1)I_L - L(\lambda_1))a\Phi]}{I_0(\lambda_2)\exp[(\kappa(\lambda_2)G(\lambda_2)T(\lambda_2)I_L - L(\lambda_2))a\Phi]}. \tag{10}$$

It is possible to simplify this expression as follows: Where λ_1 and λ_2 occur within the same spectral band, $\kappa(\lambda_1)$ and $\kappa(\lambda_2)$ may be assumed to be equivalent. If the wavelengths of consideration are not too dissimilar, we may also equate the coefficients of the unit length losses, $L(\lambda_1)$ and $L(\lambda_2)$. The overlap integrals $T(\lambda_1)$ and $T(\lambda_2)$ depend on the specific MDR excited, but in a composite spectrum where droplets take varying sizes, the identity of the resonance at wavelengths λ_1 and λ_2 will vary likewise. This will alter the overlap integrals and over a broad range of droplet sizes, it is assumed that the average overlap integral is independent of wavelength, and may thus be represented by the constant, T. The gain $G(\lambda)$ in turn depends on the species concentration and the Raman scattering cross-section. As this will be linearly proportional to the intensity of the spontaneous scatter at wavelength λ, we may replace this factor with the spontaneous scatter intensity, $I_0(\lambda)$. The following relationship may now be used:

$$\frac{I_{SRS}(\lambda_1)}{I_{SRS}(\lambda_2)} = \frac{I_0(\lambda_1)\exp[(\kappa T I_L G^* I_0(\lambda_1) - L)a\Phi]}{I_0(\lambda_2)\exp[(\kappa T I_L G^* I_0(\lambda_2) - L)a\Phi]} \tag{11}$$

where

$$G(\lambda) = G^* \times I_0(\lambda). \tag{12}$$

This can be further simplified to

$$\frac{I_{SRS}(\lambda_1)}{I_{SRS}(\lambda_2)} = \frac{I_0(\lambda_1)}{I_0(\lambda_2)} \exp[(I_0(\lambda_1) - I_0(\lambda_2))\kappa T I_L G^* a \Phi]. \tag{13}$$

The exponential dependence of the intensity ratio on the circulating laser intensity and on the spontaneous Raman scattering intensity can now be easily identified.

From equation (13), the intensity of SRS at a particular wavelength λ relative to that at the intensity maximum, λ_{max}, is given by

$$\frac{I_{SRS}(\lambda)}{I_{SRS}(\lambda_{max})} = \frac{I_0(\lambda)}{I_0(\lambda_{max})} \exp[(I_0(\lambda) - I_0(\lambda_{max}))G'] \tag{14}$$

where G' absorbs all of the constants in equation (13). For a normalized SRS spectrum for which the maximum intensity is 1 when compared with a normalized spontaneous spectrum, this can be written as:

$$I_{SRS}(\lambda) = I_0(\lambda) \exp[(I_0(\lambda) - 1)G']. \tag{15}$$

Thus, scaling a normalized spontaneous spectrum, $I_0(\lambda)$, according to this expression with a variable gain G' should allow the consistency of the SRS and spontaneous Raman spectra to be assessed.

To test the exponential scaling with incident intensity and consequently circulating intensity, we acquired composite droplet spectra using a range of incident intensities. The spectra and a plot of the intensity ratio at the two different Raman wavelengths of 641.8 and 650 nm, corresponding to Raman shifts of 3216 and 3412 cm^{-1} in the OH stretching vibration, are shown in figure 18. Where a low irradiance is used, the band contour reflects the expected exponential scaling of the spontaneous behaviour according to equation (15). In this regime, it is possible to model the SRS spectra from a suitably scaled spontaneous spectrum [117]. Figure 19 shows the lowest irradiance spectrum from figure 18 overlaid by scaled spontaneous spectra with different gains according to equation (15). Excellent agreement is obtained and indicates that the environment probed by SRS is spectroscopically indistinguishable from that probed by spontaneous Raman spectroscopy [37].

In the limit of high irradiance, the behaviour significantly departs from that predicted by equation (15). Two quite distinct maxima are observed in the SRS. Similar spectra displaying two separate peaks have been observed previously [118]. At high irradiance, the Raman gain is sufficiently large that pump depletion occurs, leading to considerable distortion of the band shape [37, 109, 117]. Unlike the measurements at low irradiance, the spontaneous band shape is no longer consistent with that observed in the SRS

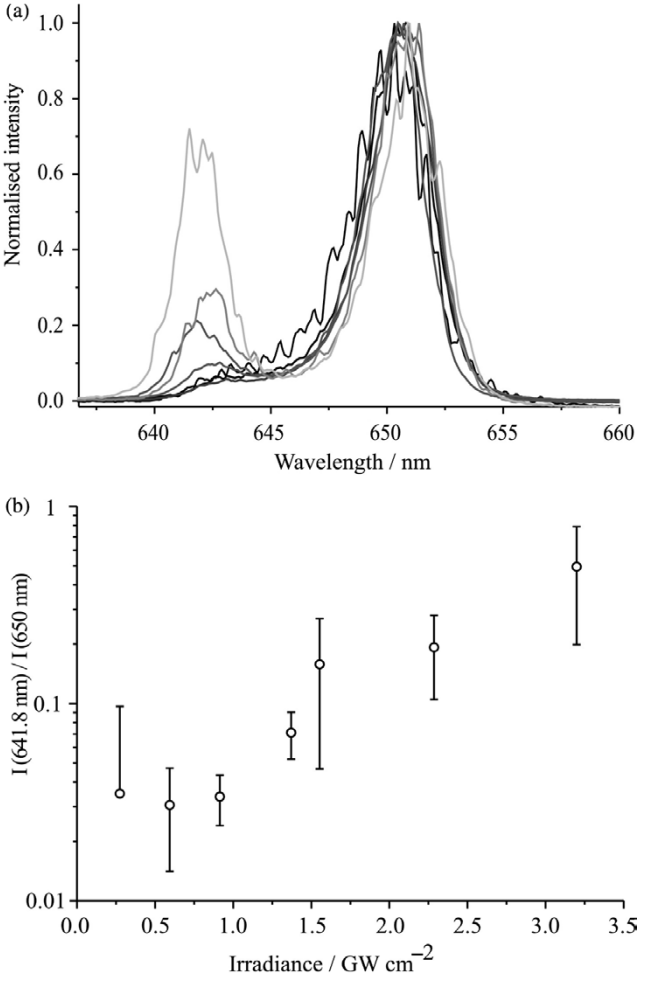

Figure 18. (a) Composite SRS spectra normalized to the band peak intensity obtained at varying incident irradiance (in sequence of solid black line becoming proressively grey: 0.3, 0.6, 0.9, 1.4, 1.6, 2.3, and 3.2 GW cm^{-2}). (b) Plot of the intensity at 642 nm (normalized to the band maximum) as a function of the irradiance. This is recorded with an excitation wavelength of 532 nm.

measurements, as illustrated in figure 20. Although the low irradiance SRS spectrum is consistent with a scaling of the spontaneous Raman band shape, the split band nature of the SRS spectrum arising at high irradiances cannot be simulated from a scaling of the spontaneous band.

The consistency of the spontaneous Raman scattering and SRS signatures at low irradiance can be further investigated by examining the dependence of the SRS OH stretching band shape on sodium chloride concentration, analogous measurements to those described earlier for spontaneous scattering. It should be expected that the behaviour evident in the SRS spectra will follow that of the bulk, i.e. a shift of the water

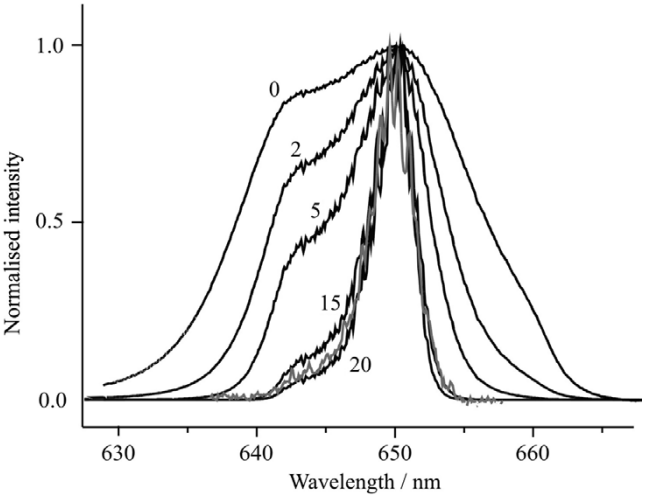

Figure 19. Comparison of the composite droplet SRS spectrum (grey line) with spontaneous spectra scaled by different gains (black lines, gains as quoted). This allows the consistency of the band shape from SRS measurements and spontaneous Raman bulk phase measurements to be assessed. This is recorded with an excitation wavelength of 532 nm.

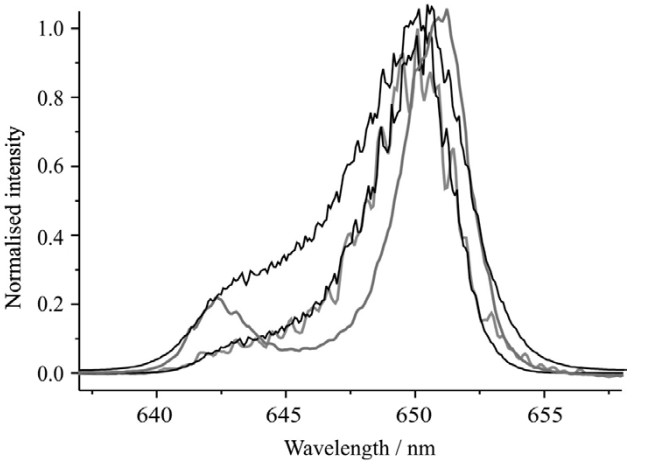

Figure 20. At low laser irradiance (0.3 GW cm^{-2}), the droplet SRS (grey) and scaled bulk phase spontaneous Raman (black) measurements are consistent. However, at high laser irradiance (2.3 GW cm^{-2}) the SRS band is distorted with the appearance of two distinct peaks. At this irradiance, the SRS bandshape cannot be reproduced from a simple scaling of the bulk phase spectrum. This is recorded with an excitation wavelength of 532 nm. [Ref. 37 – Reproduced by permission of the PCCP Owner Societies]

band λ_{max} to higher wavelength and a decrease in the intensities of the low frequency components relative to the high frequency components should occur with increasing concentration of the salt [50, 119]. Figure 21 shows SRS spectra from sodium chloride solutions between 0 and 4 M, together with overlaid bulk phase spectra. As anticipated, the spectral shift to longer wavelength in the droplet samples follows that of the bulk.

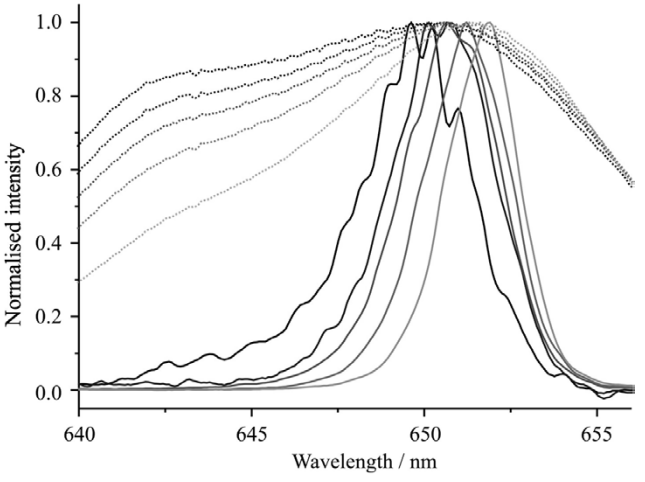

Figure 21. The dependence of the OH band shape on sodium chloride concentration for bulk phase spontaneous Raman scattering measurements (dotted lines) and SRS droplet measurements (radii ~27 μm and incident irradiance ~0.4 GW cm^{-2}, solid lines). The change in the band shape with salt concentration is shown (Black to grey: pure water, 0.5 M NaCl, 1 M NaCl, 2 M NaCl, 4 M NaCl). This is recorded with an excitation wavelength of 532 nm.

It is also apparent that the intensity of the normalized droplet spectra in the region of the shoulder in the bulk phase (~642 nm) is very low, indicating that the exponential factor must be large.

To investigate more rigorously the consistency of the SRS and spontaneous measurements, the bulk phase aqueous sodium chloride spectra must be scaled according to equation (15) to mimic those obtained from the droplets. The results of this process are shown in figure 22 for droplets of pure water and droplets of 4 M NaCl solution. The agreement in band shape is excellent and a constant gain factor is required for all salt solutions, showing no systematic dependence on salt concentration [37]. This again confirms that the environments from which the two spectra have been obtained must be the same.

Consistency between the scaling of the spontaneous Raman band and the SRS spectrum does not hold in two cases. The scatter detected from the droplets must be free from light due to other processes such as laser-induced breakdown (LIB) [120, 121], four-wave mixing (FWM), and the effects of self-focusing and self-phase modulation. Further, and less obvious, is that regardless of the polarization used for the droplet experiments, the bulk phase spectrum used in the scaling must be that acquired with a vertically polarized pump. This requirement is rather more subtle and requires explanation.

We first consider the effect of the polarization of both the incident radiation and that collected for analysis on the shape of the SRS band. This is considered in figure 23. Illumination with light of horizontal polarization leads to the excitation of TM modes in the horizontal plane and the detection of horizontally polarized scatter at the detector, which sits in the horizontal plane. Excitation of TE modes leads only to SRS that propagates in the vertical plane and is not observed at the detector.

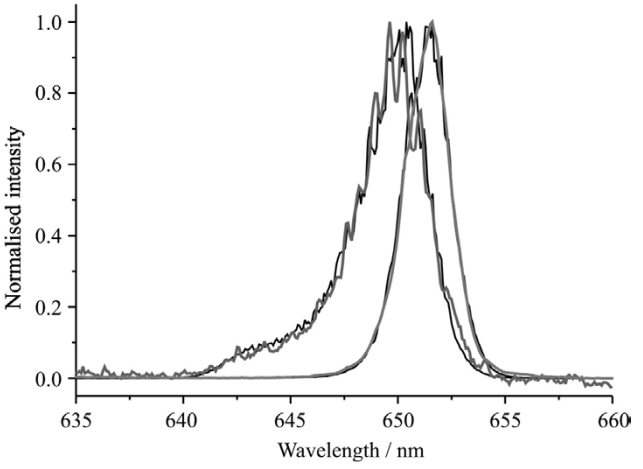

Figure 22. Comparison of the consistency between scaled spontaneous Raman bulk phase measurements (black) and droplet SRS measurements (grey, radii ~27 μm and incident irradiance ~0.4 GW cm^{-2}) with change in sodium chloride concentration (left spectra pure water, and right spectra 4 M). The gain factors are 17.12 and 14.72 for the pure water and 4 M solution, respectively. This is recorded with an excitation wavelength of 532 nm. [Ref. 37 – Reproduced by permission of the PCCP Owner Societies]

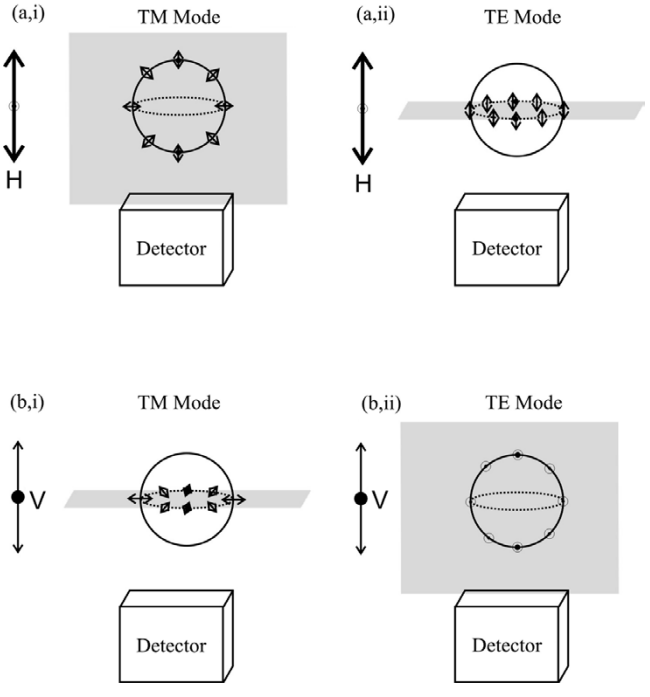

Figure 23. A schematic of the dependence of the scattering polarization detected on the illuminating polarization and WGM polarization excited, viewed from above. The plane in which the light is scattered is indicated by the grey shaded area. In (a,i) and (a,ii), the incident polarization is horizontal. Only scatter from TM modes is observed in the horizontal plane and reaches the detector (a,i). In (b,i) and (b,ii), the incident polarization is vertical. Only scatter from TE modes is observed in the horizontal plane and reaches the detector (b,ii).

Conversely, excitation of TE modes with vertically polarized light leads to the collection of vertically polarized scatter at the detector. TM modes excited with vertically polarized incident light lead to scatter in the vertical plane which is not collected. Thus, SRS collected in the horizontal plane arises from the collection of scatter from TM modes, when the incident polarization is horizontal, and vertical scatter from TE modes when the incident polarization is vertical. In both cases, the scatter will have a form consistent with a parallel spontaneous Raman band, observed when collecting vertically polarized light scattered from a bulk sample illuminated with vertically polarized laser light.

A demonstration that the parallel scattering spontaneous spectrum must be used to model the SRS scatter is illustrated in figure 24. In figure 24(a) we have attempted unsuccessfully to fit the bulk phase spectrum obtained with a horizontally polarized incident beam, at a pump wavelength of 355 nm, to a droplet spectra acquired with the same source polarization. The spontaneous band from the bulk phase measurements shows the anisotropic component alone, lacking the pronounced low frequency shoulder at $\sim 3200\,\mathrm{cm}^{-1}$ (a wavelength of ~ 401 nm) evident in the spectrum in figure 8(c). At high gain, the shoulder is under-estimated, whereas at low gain, the shoulder is better approximated, but the width of the peak is wildly over-estimated. In contrast, a droplet spectrum obtained using a horizontally-polarized beam has been compared with a scaled bulk phase spectrum obtained using a vertically polarized beam in figure 24(b). The good agreement attests to the veracity of the argument that the SRS spectrum acquired by a detector in the horizontal plane with a horizontal pump beam, initially expected to show only the anisotropic component of the OH band, must be counter intuitively compared to the spectrum acquired with parallel incident and scattered polarizations.

A further and final demonstration of the quasi-forwards nature of the scatter detected in SRS from droplets is given in figure 25. The absolute peak intensity of the water band has been plotted as a function of the incident polarization (or waveplate orientation angle) for different analyser polarizations. When the incident polarization is vertical, the waveleplate angle is 0 or 90° and when the incident polarization is horizontal, the waveleplate angle is 45°. Parts (a) and (b) refer to SRS spectra (and hence have extremely large errors associated with the absolute intensities), and (c) refers to bulk phase spontaneous measurements. The SRS signal intensity is at a maximum when the incident illumination is horizontally polarized and when the analyser is set to accept horizontally polarized scatter, reflected by the maximum in intensity in figure 25(a). This again is consistent with the parallel scattering component reaching the detector, even though in a traditional Raman measurement this would be considered to give the perpendicular component. Conversely, the signal intensity is at a maximum with vertically polarized incident light when the analyser is set to accept vertically polarized light, as reflected by the maxima in intensity in figure 25(b). Thus, the SRS trends in figures 25(a) and (b) are consistent with the trend observed in the parallel polarization collection of spontaneous scatter, shown in figure 25(c). Hence, in any comparison of spontaneous and SRS spectra, it is necessary always to use those spontaneous spectra in which scatter due to the isotropic part of the polarizability has been detected.

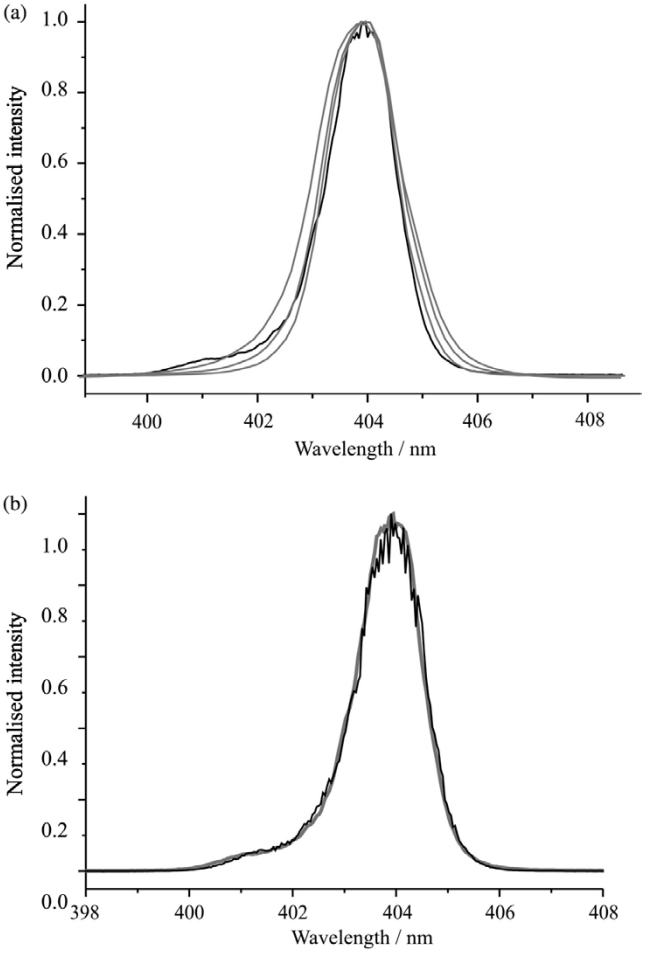

Figure 24. Examination of the SRS signature when illuminated with horizontally polarized light and no polarization selection of scattered light. (a) The SRS spectrum from droplets (black line, radii ~30 μm) is inconsistent with the scaling of a spontaneous spectrum recorded with a horizontally polarized incident beam and unpolarized collection [Z(X, Y + Z)X] (increasing gain coefficieint with decreasing spectral bandwidth). The data was collected using 355 nm excitation and an incident irradiance of 0.55 GW cm^{-2}. (b) The SRS droplet spectrum is instead consistent with a scaled spontaneous band recorded with vertically polarized illumination (gain factor 12.5) and unpolarized collection [Z(X, Y + Z)X] (grey line).

4.4. *Determining the composition of multicomponent aerosol droplets by SRS*

To detect specific components within an aerosol droplet by SRS two conditions must be satisfied [52, 109, 122, 123]. Firstly, the component must be present at a sufficiently high concentration that the threshold condition, equation (8), is satisfied. The spontaneous Raman intensity must surpass the threshold intensity required for SRS to occur. This typically imposes detection limits on detecting minor components that are higher than those determined from spontaneous Raman scattering. As described above, the limits for detecting nitrate and sulphate are at the mM level from spontaneous

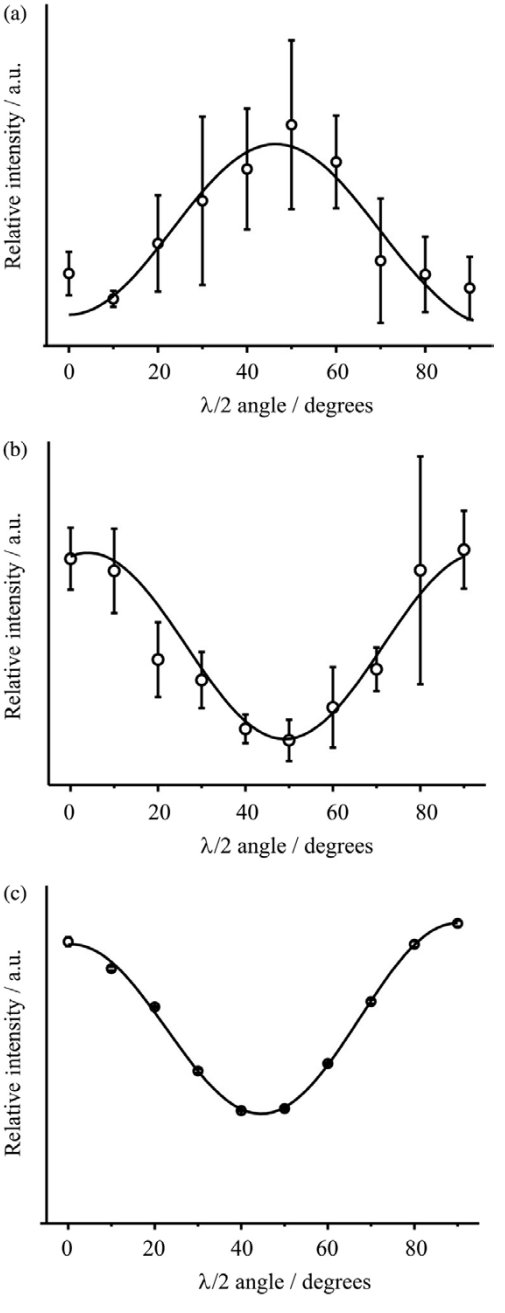

Figure 25. Dependence of the scattered light intensity with change in incident polarization, vertical polarization at an angle of 0°: (a) intensity of horizontal polarization of SRS; (b) intensity of vertical polarization of SRS; (c) intensity of vertical polarization of spontaneous scatter.

scattering [79, 111]. However, from SRS the limits are considerably higher (> 0.1 M) [109, 123]. This restricts the applicability of SRS for compositional determination. Strategies for circumventing this problem have been investigated using optical seeding techniques and this will be returned to in the following section [124–130].

A second condition that must be satisfied to observe SRS is that a WGM must exist within the spontaneous Raman band of the component. For components such as water with a broad OH stretching band, this condition is always satisfied for droplets larger than 1 μm in radius. For components such as nitrate and sulphate with linewidths of <1 nm for their Raman active symmetric stretching vibrations, this resonance condition is satisfied less frequently with decreasing droplet size. The stringency of the resonance condition is illustrated in figure 26, where the condition is compared for the symmetric stretching vibration of sulphate and the OH stretching vibration of water for two droplet sizes. Clearly, if the resonance condition is not satisfied, the spectroscopic technique will be blind to the chemical constituent.

We have studied the effect of the resonance condition on the detection efficiency of nitrate and sulphate in aqueous droplets, when the concentration of the anion is sufficient enough that the threshold condition is always satisfied. Figure 27 shows the fraction of droplets observed to satisfy the resonance condition for the detection of sulphate and nitrate with varying droplet size when compared to the total number of droplets showing some signal. With increasing size, the nitrate and sulphate are more frequently detected as the mode density increases and the resonance condition is more frequently satisfied. Further, the symmetric stretch of the nitrate ion has a linewidth of 0.31 nm, marginally wider than that of sulphate, 0.28 nm, and is consistently detected more frequently.

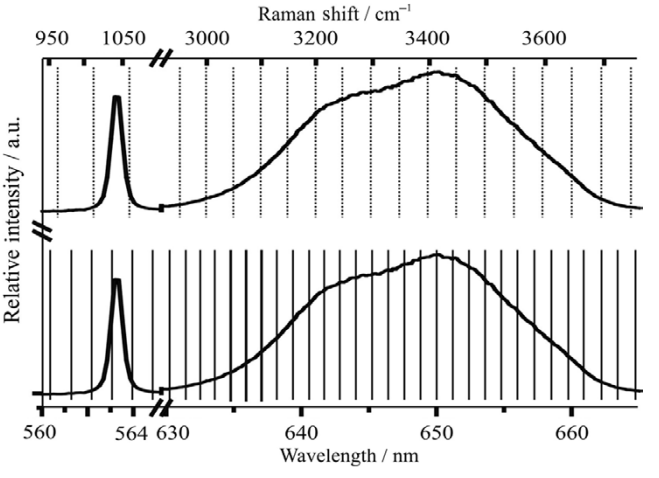

Figure 26. Schematic of the resonance condition that must be satisfied to detect the sulphate ion in aqueous droplets (top spectrum, a 24 μm radius droplet; bottom spectrum, a 42 μm radius droplet). An excitation wavelength of 532 nm is assumed. The probability of a resonance lying within the spontaneous linewidth of the sulphate band decreases with decreasing droplet size. By contrast, the probability of a resonance within the spontaneous linewidth of the water band is invariant. [Ref. 109 – Reproduced by permission of the PCCP Owner Societies]

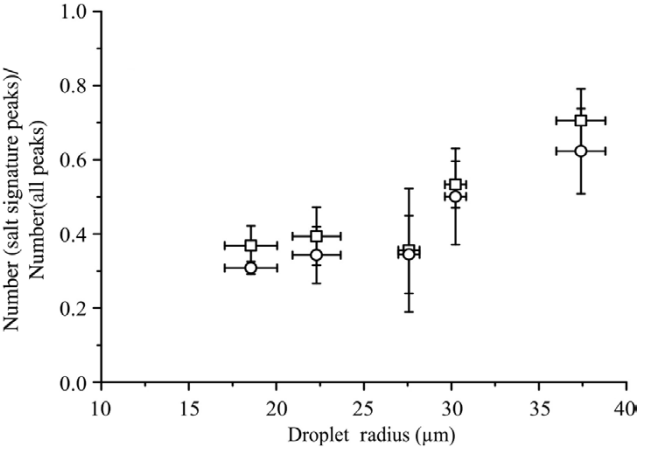

Figure 27. Fraction of droplets showing a signature from the nitrate (squares) and sulphate (circles) ions that show SRS from water. The resonance condition is satisfied more frequently with increasing droplet size and the ion appears as a signature in the SRS spectrum with higher frequency.

If both the resonance and threshold conditions are satisfied, the SRS intensity for a particular component is dependent on the concentration in a non-linear manner [52, 109, 131]. This should be contrasted to the linear dependence of signal intensity on species concentration observed from linear Raman scattering [111] and illustrated in figure 11. The non-linear dependence of signal intensity on concentration is illustrated in figure 28 for the detection of ethanol in ethanol/water droplets. The signal from the CH stretching vibration of ethanol increases exponentially with increasing ethanol concentration relative to the signal from the OH stretching vibration from the dominant water component [52]. The exponential growth in signal with concentration affords an extremely sensitive method for determining small changes in droplet composition provided the threshold condition is satisfied. For example, at an excitation wavelength of 355 nm, the CH band intensity changes by two orders of magnitude for a change in composition of ethanol from 16% v/v to 18% v/v. We have used this technique to examine the small changes in composition that occur during the evaporation of alcohol/water droplets [26, 29, 51].

The Raman cross-sections of different components are wavelength dependent. Thus, the threshold for detecting a particular component will depend on the wavelength of the excitation laser. This is illustrated in figure 28 for the detection of ethanol. At the longer excitation wavelength of 532 nm, the Raman cross-section of ethanol with respect to water is larger than at 355 nm [52]. Thus, the threshold for detecting the organic component occurs at a lower threshold concentration.

At high gains, the intensity of SRS can surpass a threshold for pumping higher order Raman processes [132–135]. Thus, the first-order Raman scattering is sufficiently intense to act as a pump source, leading to the observation of second-order Raman scattering at one further Stoke's shift from the first-order peak. This can act as a further pump source leading to higher order processes: indeed, a 17th order Raman scattering process has been reported [134]. We illustrate an example of high-order Raman

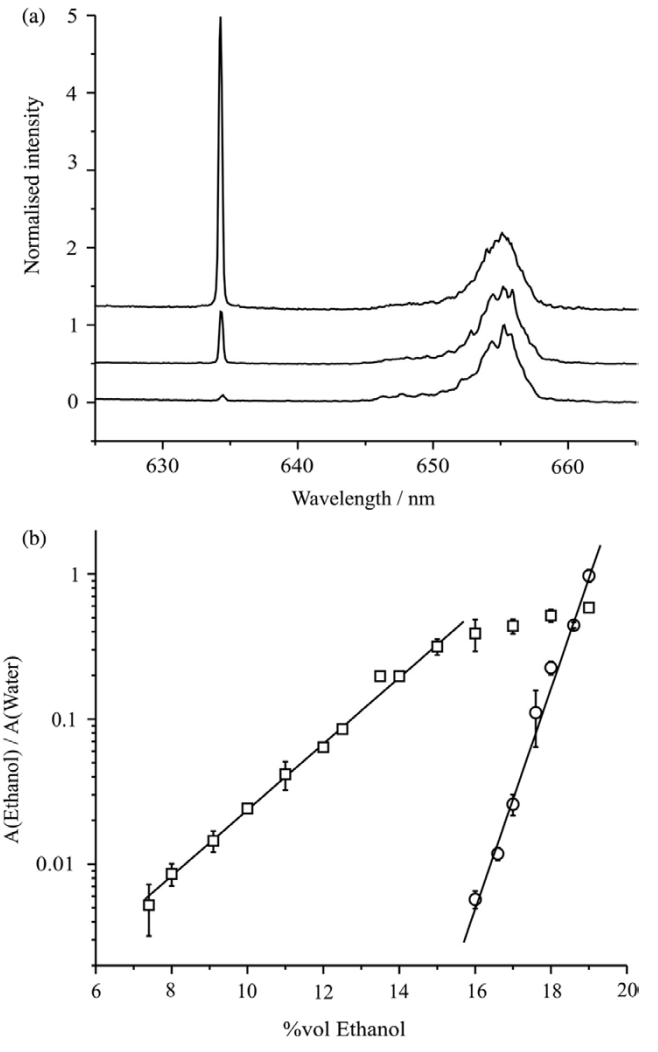

Figure 28. (a) SRS composite spectrum accumulated from ~1000 ethanol/water droplets with compositions of 15, 12, 8% v/v (top, middle and bottom spectra, respectively). The intensity of the CH stretching vibration signature decreases with decreasing concentration. The excitation wavelength is 532 nm. (b) Calibration curves for the integrated intensity (area) of the CH signature relative to the water OH band for ethanol/water droplets recorded at excitation wavelengths of 532 and 355 nm (squares and circles, respectively). [Reprinted from Ref. 52, with permission from Elsevier]

generation in figure 29 observed in the Raman scattering from nitrate present in aqueous droplets of sodium nitrate at a concentration of 1.6 M [109]. The nitrate first-order Raman scattering at 563 nm is sufficiently intense to act as a pump source for Raman scattering from both nitrate and water, leading to the appearance of bands at ~598 nm and ~700 nm. Further, the 598 nm second-order nitrate band is sufficiently intense to pump third-order Raman scattering from nitrate appearing at ~639 nm. The first-order water band shows considerable distortion with the appearance of two peaks,

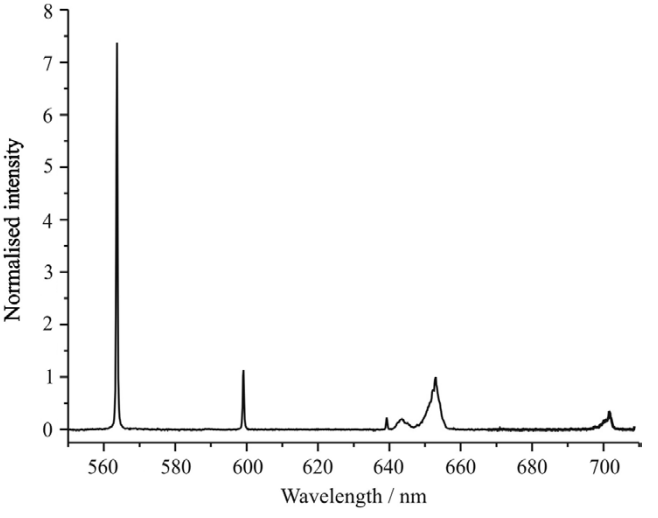

Figure 29. Spectrum showing the appearance of high order SRS from aqueous nitrate droplets (1.6 M, ~31 μm in radius) at a laser intensity of 1.7 GW cm^{-2}. This is recorded with an excitation wavelength of 532 nm. The first-order band appears at ~563 nm, the second order at ~598 nm, the third order at ~639 nm. [Ref. 109 – Reproduced by permission of the PCCP Owner Societies]

reflecting the high laser irradiances within the droplet which are required to pump these high order processes.

4.5. *Optical seeding and manipulating the threshold condition*

We have highlighted that the threshold condition imposed on SRS leads to detection limits for minor components that are inferior to those observed from spontaneous Raman scattering. However, an advantage of SRS probing is that a spectroscopic signature of the size and composition of a single droplet can be achieved with a single nanosecond laser pulse, compared to the sampling and signal acquisition times of ~1 second that are required to achieve sufficient spontaneous Raman scattering signal for droplet characterization. As described above, the threshold concentration can be tuned to a certain extent by varying the probe wavelength. Further, within a limited range, the illumination pulse energy can be increased to lower the detection threshold. However, optical saturation and LIB limit the upper laser fluence that can be applied without significantly perturbing the droplet or introducing ambiguity into the spectroscopic measurement [123]. We will now explore the possibility of varying the threshold concentration through the application of a second laser pulse of different colour to the pump laser [124–130] to seed the droplet and assist in surpassing the threshold intensity of light at the Raman wavelength at a lower component concentration [126, 130].

One approach to improve the detection sensitivity of the minor component by SRS is to apply two pump sources at different frequencies, such that the Stokes shifted majority species band produced by one pump source spectrally overlaps with the Stokes shifted minority species band produced by the second pump source. In this case, the

light from the majority species acts as seed radiation, providing a background upon which spontaneous scatter of the minority species can build allowing it to surpass threshold [126, 130]. In this way the SRS threshold for the minority species may be reached at lower number densities, improving the detection limit. With this approach, not only is the intensity of the minority species scatter enhanced, but also the ability to characterize droplets based on the properties of WGMs is preserved by recording all chemical constituents in the same spectral window with high wavelength resolution. This could allow the concentrations of a number of species to be simultaneously quantified and the droplet size to be determined.

In this review, we report seeding studies conducted on droplets containing sodium nitrate as a minority species and water as a majority species. Droplets were generated by a VOAG and measurements were performed using the experimental layout described in section 2.1 with the addition of an interrogation source, a dye laser operating between 606 nm and 613 nm in wavelength. Operating in this wavelength range, first-order Stokes scatter from nitrate occurs between 647 and 655 nm. As in our earlier measurements, illumination at 532 nm with a Nd:YAG laser was used to generate SRS from the OH stretching band of water covering the wavelength range 647 to 656 nm. Thus, the OH SRS provided a background intensity on which the first-order Stokes scatter from the nitrate could build, allowing it to surpass threshold for SRS at a lower concentration than in single colour SRS.

Additional laser path length was created to control the time of arrival of the two laser pulses at a droplet. Since WGMs have lifetimes of the order of nanoseconds within a droplet, the path lengths of the two laser pulses were varied such that the 532 nm pulse was incident upon a droplet approximately 6 ns before the interrogation pulse. By delaying the dye laser pulse relative to the 532 nm pulse we ensured that the WGMs produced by the seed pulse were already present and remained excited at the time of arrival of the dye laser pulse. In addition, delaying the dye laser pulse reduces the occurrence of LIB of the droplet that occurs if both of the laser pulses are delivered simultaneously.

The seeding effect is illustrated in figure 30 for 35 μm droplets at a nitrate concentration of 1.5 M. A significant increase in the intensity of the SRS nitrate scatter is observed when both the 532 nm and dye laser pulses are incident upon a droplet over that observed when only the dye laser pulse is incident. In this measurement, the dye laser wavelength was set at 610 nm, resulting in first-order nitrate scatter at 652 nm from the υ_1 nitrate vibration with a 1049 cm^{-1} Stokes shift. It is clear that the seeded spectrum is not simply the sum of the intensities of the scattering from nitrate and water, but is the result of non-linear optical mixing processes occurring within the droplet. The seeded intensity is so great, it almost completely suppresses the SRS OH band.

As the dye wavelength is tuned between 606 and 613 nm, the first-order nitrate Raman scattering peak is translated in wavelength across the breadth of the OH stretching band. Thus, it is possible to compare the extent of optical seeding arising at different points within the intensity profile of the OH band, as illustrated in figure 31. As the nitrate peak is positioned in the region away from the spectral maximum of the OH band, no seeding effect is observed. As the nitrate band is shifted in wavelength to fall within the OH band, the seeding effect appears and becomes more pronounced as

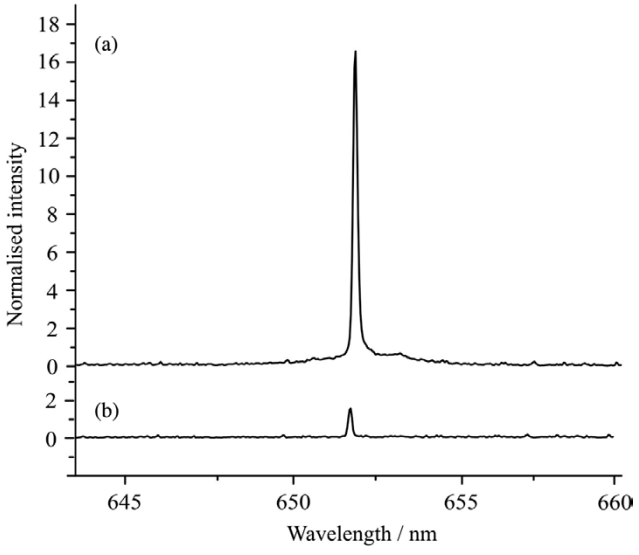

Figure 30. An illustration of the SRS signal arising from the nitrate anion excited from a wavelength of 610 nm, with seeding (a) and without seeding (b). The anion concentration is 1.5 M and the droplet radius is ~35 μm. In spectrum (b), only the dye excitation pulse illuminates the droplet and a weak nitrate signature results. In spectrum (a), the 532 nm laser pulse leads to SRS from the OH stretching band of water, apparent in the spectrum. This leads to the seeding of the nitrate Raman signal at 652 nm and an enhancement of the signal from the nitrate species.

the nitrate peak is moved to the most intense wavelength of the OH scatter where the seeding is strongest. Further, an enhancement factor can be calculated using the ratio of the intensity of the nitrate scatter recorded when both 532 nm and dye pulses are incident upon a droplet, compared to the intensity of nitrate scatter recorded when just the dye pulse is applied and no seeding radiation is present. Figure 32 shows that the enhancement factor variation, which follows the intensity trend of the OH band and confirms the effect of the seeding scatter intensity on the nitrate signal enhancement. A large error in enhancement in figure 32 arises from the variations of the laser illumination position on a droplet.

5. Probing the evolving size and composition of aerosol droplets

We have discussed in detail the spectroscopic techniques that can be used to characterize the size and composition of liquid aerosol droplets 1–120 μm in diameter. We now turn out attention to review some studies of aerosol dynamics in which we have applied these techniques. We begin by considering investigations of the evaporation of volatile alcohol/water droplets [26, 29, 51], before reviewing measurements of the thermodynamic properties of aerosol droplets [63], and we finally consider studies of aerosol coagulation [136].

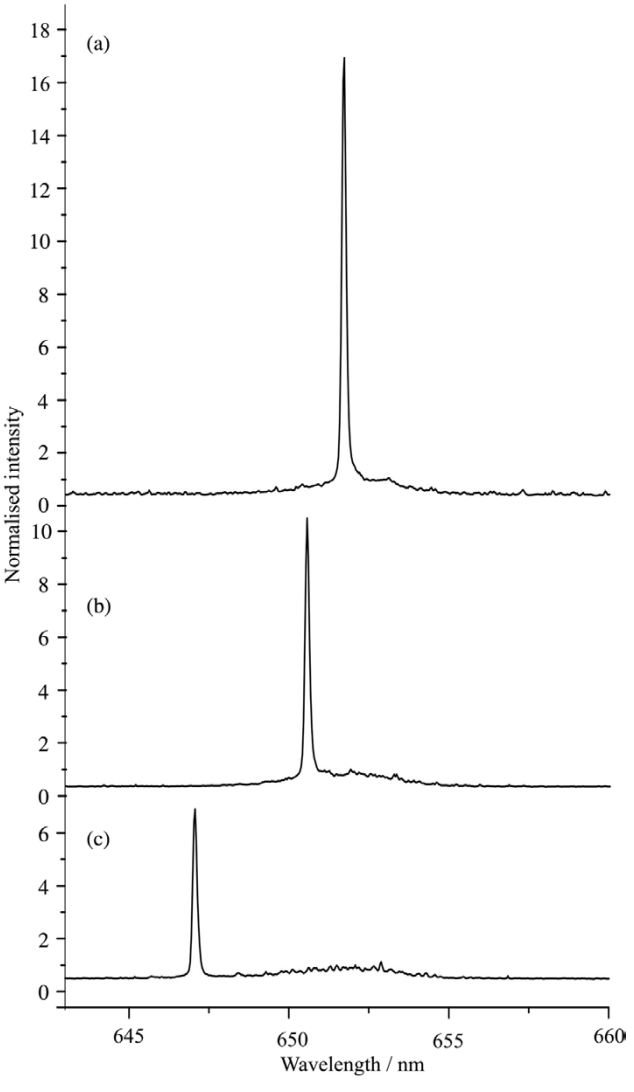

Figure 31. The variation in nitrate SRS intensity with excitation dye wavelength: (a) 610 nm, (b) 609 nm and (c) 606 nm. The nitrate signal is most intense in (a); the nitrate band is most strongly seeded when its SRS band falls at the maximum intensity of the OH SRS band.

5.1. *Volatile droplet evaporation*

In characterizing the evaporation dynamics of volatile droplets, we have shown that SRS can provide a signature of the evolving droplet size, composition and temperature during evaporation [26, 29, 51]. Further, the composition and temperature of a droplet are measured in the volume sampled by the circulating WGMs, near the droplet surface, and the SRS signal shows an exponential scaling with component concentration.

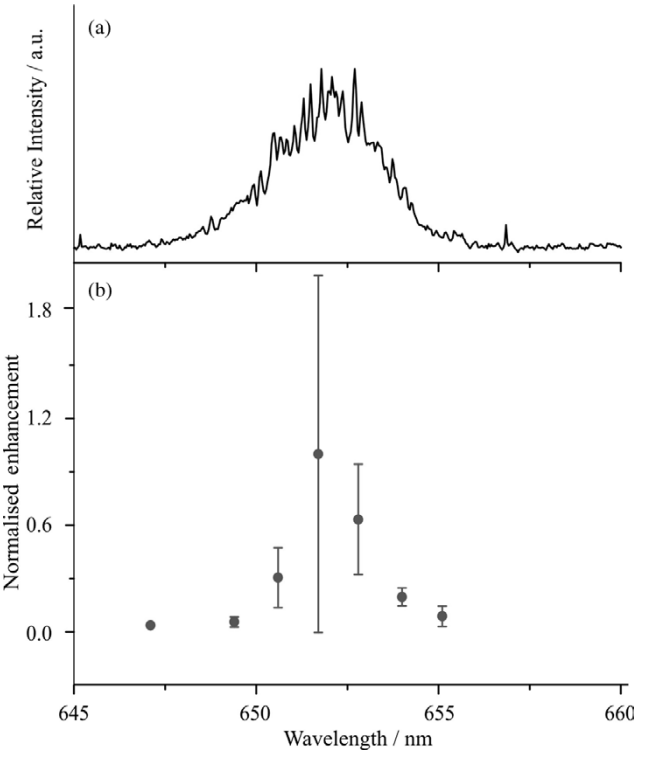

Figure 32. The magnitude of the seeding enhancement (part (b)) is observed to be at a maximum when the nitrate SRS band falls at the maximum intensity of the OH SRS band, shown in spectrum (a).

These factors combine to provide a sensitive probe of droplet evaporation. We have also demonstrated that LIF can be used to characterize the volume averaged temperature of an evaporating droplet, providing a strategy for examining inhomogeneities in droplet temperature during evaporation.

Evaporation studies have concentrated on the evaporation of alcohol/water droplets, composed of methanol/water, ethanol/water and 1-propanol/water [26, 29, 51]. Droplets are generated by a VOAG and SRS measurements are performed according to the strategy described in section 2.1, with the addition that studies are performed in an aerosol flow chamber [60]. This allows the regulation of surrounding gas phase pressure and composition. Studies have examined the evaporation of droplets initially 23–60 μm in radius over timescales of 200 μs to 12 ms at surrounding nitrogen gas pressures of 7–100 kPa. For these droplet sizes and at these pressures, the evaporation rate is determined by the rate of mass and heat transfer in the gas phase [24].

An example of the temporal variation in droplet composition, size and temperature during the evaporation of ethanol/water droplets is shown in figure 33. The initial droplet of radius is 40.2 μm has a composition of 18.6% v/v ethanol, with the remainder water. The ethanol component has a higher vapour pressure than the water component and evaporates more rapidly into the dry nitrogen surrounding the droplet at a pressure of 77 kPa. Thus, over the first 4 ms of evaporation, the concentration of ethanol

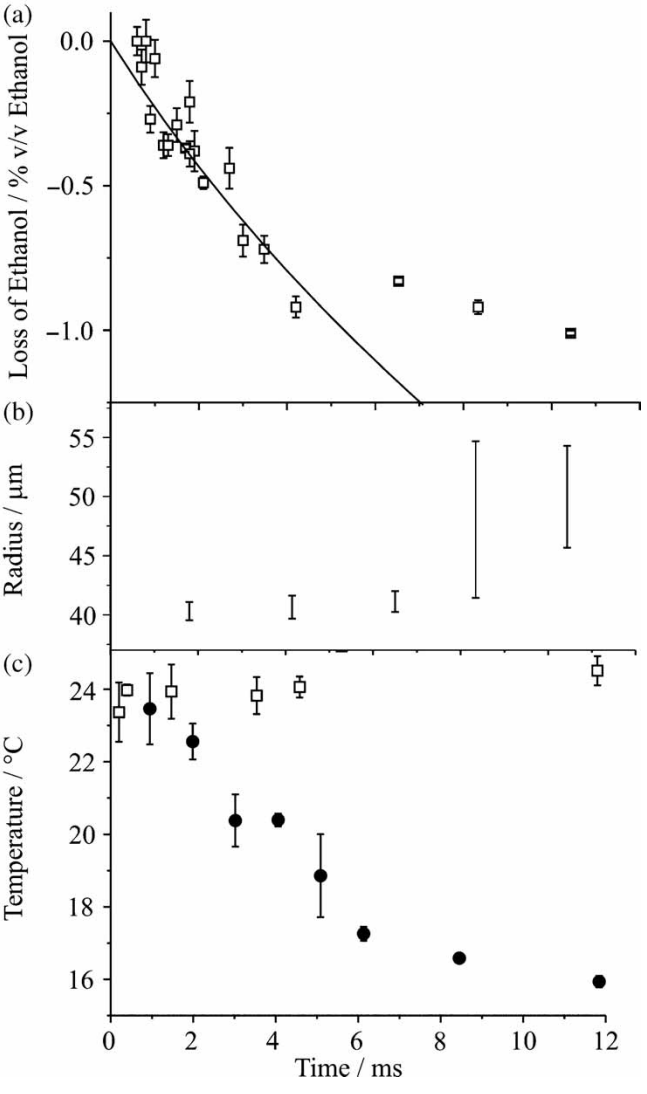

Figure 33. Change with time of droplet (a) composition, (b) size, and (c) temperature during the evaporation of ethanol/water droplets, initially 18.6% v/v ethanol and 40.2 μm in radius, at a surrounding gas phase pressure of 77 kPa. The coagulation of droplets in the droplet train is evident at times longer than 6 ms, with a corresponding increase in droplet size and decrease in evaporation rate. The change in composition is compared with a calculation based on a quasi-steady treatment, shown by the solid line. A larger change in droplet temperature is observed when the evaporation occurs at a lower surrounding gas pressure of 7 kPa (filled circles), compared to 77 kPa (squares). [Reprinted with permission from ref. 51. Copyright 2005 American Chemical Society]

falls rapidly. The evolution in droplet size cannot be determined with sufficient accuracy to investigate the size changes accompanying evaporation. This is primarily a consequence of the polydispersity of successive droplets sampled [103]. However, at times later than 6 ms, the size of the droplet becomes larger by $>10\,\mu m$ and the

composition of the droplets probed shows no further change. At these late times, droplet coagulation within the droplet train occurs, leading to a marked increase in droplet size and a significant decrease in the mass transfer rate due to a reduction in the surface-to-volume ratio.

At a surrounding gas pressure of 77 kPa, the rate of mass transfer is sufficiently slow that evaporative cooling is not significant. However, at a surrounding gas pressure of 7 kPa, gas diffusion of volatile components away from the droplet surface is considerably more rapid [29]. The temperature of the droplet decreases markedly (figure 33c) as the more energetic molecules evaporate from the droplet and the droplet undergoes unsteady evaporation [24, 25, 27, 137, 138]. The evaporative cooling cannot be balanced by heat transfer from the surrounding gas phase or internally within the droplet. The droplet surface cools, lowering the vapour pressure of the components, and slowing the mass transfer rate. Eventually, the rate of mass transfer is expected to become constant as the temperature of the surface becomes constant.

The measurements of evolving composition and temperature can be compared with the predictions of a quasi-steady model, which accounts for the temporal variation in droplet temperature and composition and allows the time-dependent mass and heat transfer rates to be estimated [26, 28]. The model assumes that mass transfer across the liquid–gas surface is rapid compared with mass transfer in the bulk phases, ensuring that the vapour composition responds instantaneously to changes in droplet composition and temperature, i.e. equilibrium is rapidly established between the droplet surface composition and near surface gas phase composition. It is also assumed that the rate of mass and heat transfer in the surrounding gas phase is rapid compared to changes in boundary conditions, such as the composition, temperature and extent of the surface. Thus, the surrounding radial dependence of the gas phase composition and temperature can be always approximated as achieving a steady state.

To compare the model calculations with the experimental data, it is essential to recognize that the composition in the droplet is inhomogeneous on the timescales probed. Liquid diffusion within the droplet cannot maintain a homogeneous distribution of the different components. The surface region rapidly becomes depleted in alcohol, while the droplet core remains at the initial composition. The quasi-steady model yields a compositional change that reflects the much smaller overall change in composition of the entire droplet, and not the outer few microns probed by the SRS measurement. Thus, to compare the predictions and measurements, a scaling factor is empirically determined. A comparison of the qualitative trends in composition is shown in figure 33(a) for the time dependent data at times prior to droplet coagulation within the droplet train.

A further test of the model is to compare the gas-phase pressure dependent trends in composition, at a fixed evaporation time, for droplets of different initial sizes. By varying the pressure, the rate of gas diffusion is altered. At lower pressures, the gas diffusion rate is higher and the droplet changes in composition more significantly during a fixed time period. Examples of these trends are shown in figure 34 for the evaporation of ethanol/water and methanol/water droplets of two different sizes. Comparison is also made with the prediction of the model using the empirically determined scaling factor discussed above. Excellent agreement is observed between the experimental measurements and model for all systems.

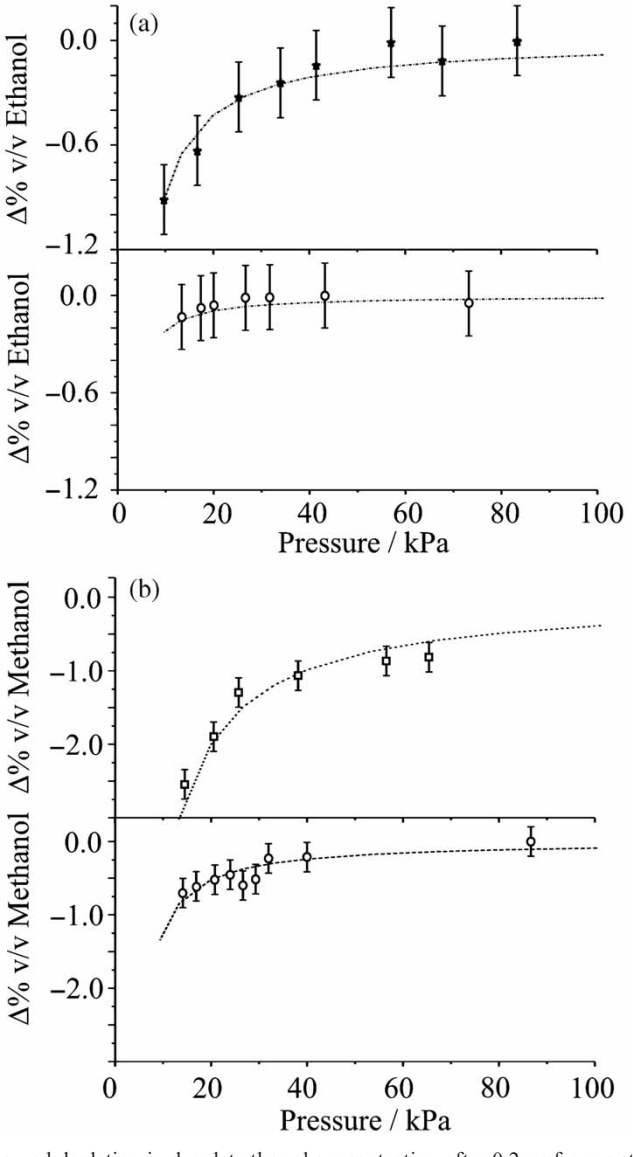

Figure 34. (a) Measured depletion in droplet ethanol concentration after 0.2 ms from a starting composition of 18.6% v/v with change in surrounding gas pressure. The top graph is for droplets initially 26 μm in radius and the bottom graph for droplets 57 μm in radius. (b) Similar pressure dependent trends for methanol/water droplets, initially 25% v/v methanol. The top graph is for droplets initially 27 μm in radius and the bottom graph for droplets 57 μm in radius. In each figure, the line represents the quasi-steady-state model prediction.

The dependence of the OH band shape on the temperature of the liquid has been described in section 3. With the significant changes in temperature expected during droplet evaporation, the shape of the SRS OH band shape can be used as a probe of near-surface temperature. An example of this is shown in figure 35 for the evaporation

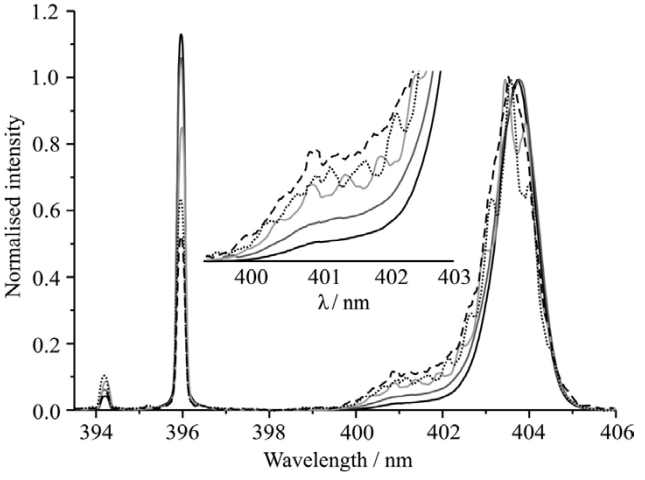

Figure 35. Change in the OH band shape during the evaporation of 25% v/v methanol droplets at a surrounding gas pressure of 20 kPa. The droplets were initially 25 μm in radius. The spectra were acquired from droplets at increasing fall times of 0.2, 0.8, 1.3, 1.3 and 2.3 ms (black, dark grey, light grey, black dotted and black dashed, respectively). This is recorded with an excitation wavelength of 355 nm. [Ref. 29 – Reproduced by permission of the PCCP Owner Societies]

of methanol/water droplets. With increasing time, the low frequency side of the Raman band becomes more pronounced [29], confirming that the near-surface temperature decreases, given the consistency between spontaneous and SRS band shapes discussed in section 3.3.

5.2. *Thermodynamic measurements of equilibrium droplet size*

We have described in the preceding section a strategy for probing the kinetics of mass and heat transfer during droplet evaporation. We now illustrate how similar techniques can be adopted to characterize the thermodynamic properties of multicomponent aerosol droplets.

Two contrasting effects govern the equilibrium size and composition of aerosol droplets and these are described by Köhler theory [12]. During the evaporation of a droplet, the effect of surface curvature on vapour pressure, referred to as the Kelvin effect, leads to an increase in the vapour pressure of the droplet. Thus, pure water droplets are unstable and require a supersaturation of water vapour (a partial pressure exceeding the vapour pressure of a flat surface) to exist in equilibrium with their surroundings. However, for any droplet containing an involatile component, a decrease in size leads to an increase in concentration of the involatile component and a decrease in the vapour pressure of the droplet. This is referred to as the solute effect. These two effects combine with the consequence that a droplet containing a specific mass loading of an involatile component will, at any particular relative humidity, reach an equilibrium size. At this size, the vapour pressure of the droplet equals the partial pressure of water present in the gas phase and an equilibrium state is reached. Thus, in order to understand the size distributions of wet particles in the atmosphere it is

essential to understand the relationship between involatile and volatile solute concentrations, and RH. To perform direct measurements of the equilibrium state of an aerosol, it is essential that the composition and the size of the droplet be accurately determined over long timescales. Combining Raman spectroscopy with aerosol optical tweezers provides a unique tool for performing these measurements [63].

As a benchmark system, we have examined the equilibrium variation of droplet size with RH for sodium chloride doped droplets. Measurements can be performed on a single droplet over timescales of days. An example of the variation in droplet size and RH for an aqueous sodium chloride droplet, initially composed of 1.28 M sodium chloride, is shown in figure 36. The size of the droplet was determined accurately from the wavelengths of the WGMs appearing in the Raman fingerprint, as described in section 4.2. The RH was determined with a RH probe located in the trapping cell within 2 cm from the trapped droplet. A comparison of the variation in equilibrium size with

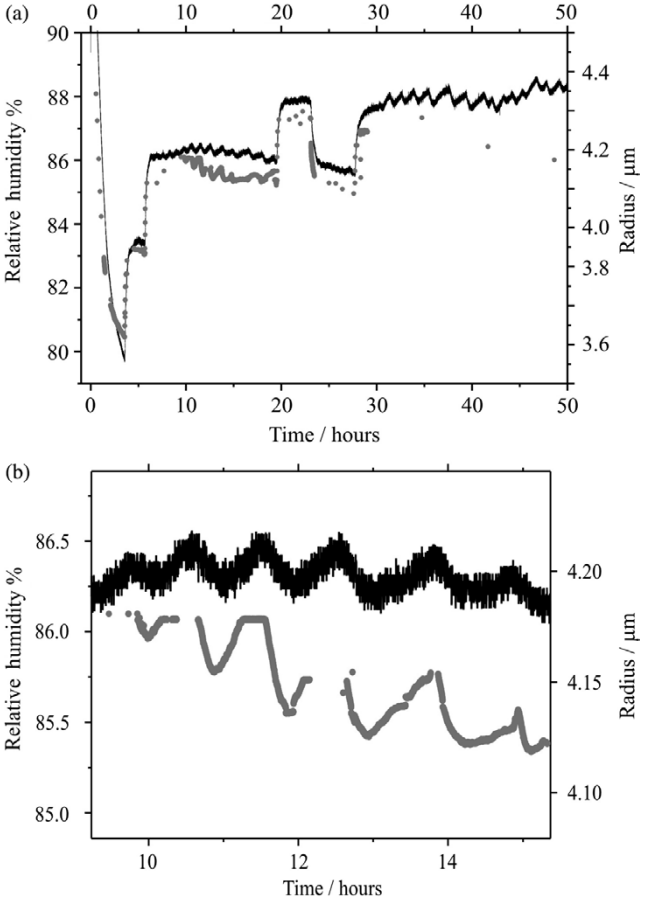

Figure 36. (a) Variation in the RH (black line) and droplet size (grey circles) over 50 hours. This illustrates the variation in equilibrium droplet size with RH for droplets containing sodium chloride at an initial concentration of ~1 M. (b) An expanded view of the RH and size variations within a 4 hour time window. [Reprinted with permission from ref. 63. Copyright 2006 American Chemical Society]

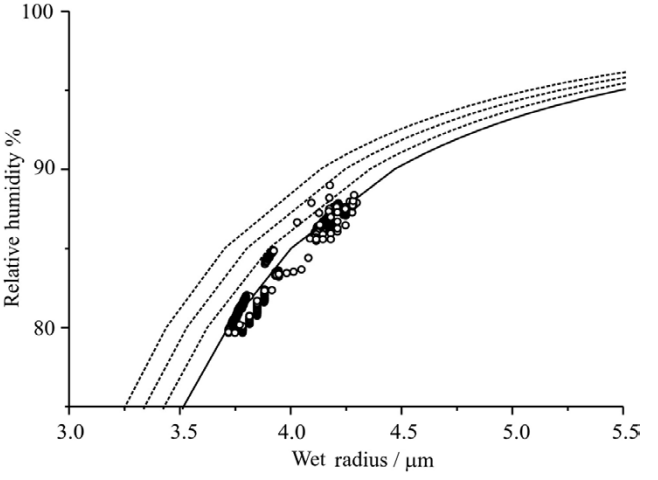

Figure 37. Comparison of the measured dependence of the equilibrium droplet size with variation in RH and that predicted from Köhler theory for aqueous/NaCl droplets. The four Köhler curves shown are for dry NaCl particles with radii of 1714, 1761, 1807, and 1853 nm (leftmost to rightmost curves, respectively). [Reprinted with permission from ref. 63. Copyright 2006 American Chemical Society]

RH with predictions from Köhler theory is shown in figure 37. The agreement between the calculations and measurements is excellent.

A problem with the measurement strategy described is the inaccuracy in determining the RH. Not only does the RH probe have a slow time response (~50 s in slow moving air), but the accuracy in the RH measurement is only ±2%. Further, the initial burst of aerosol from which the single droplet is trapped leads to the deposition of aqueous solution throughout the trapping cell, leading to RH gradients that can take many hours to abate. This can further reduce the accuracy of the measurements. A strategy for avoiding these complications has now been developed that arises from the unique advantages offered by the optical tweezing approach. Two optical traps can be formed in parallel, a few tens of microns in separation. Thus, a control droplet can be trapped in one optical trap, while the droplet with the composition of interest can be trapped in a second optical trap. By simultaneously recording the evolution in both droplet sizes, the control droplet can act as a highly accurate and local probe of RH, allowing the thermodynamic properties of the second droplet to be directly investigated [139].

5.3. *Probing the coagulation of aerosol droplets*

Characterizing equilibrium particle size and composition allows us to tackle many of the challenges in aerosol science highlighted in the *Introduction*. The influence of different inorganic and organic components on equilibrium size and composition can now be routinely investigated. However, the influence of component mixing state on the thermodynamic properties and kinetics of chemical and physical transformation is of crucial importance. To fully explore the equilibrium properties, it is essential to understand the behaviour of multiphase aerosols, the segregation of an organic phase

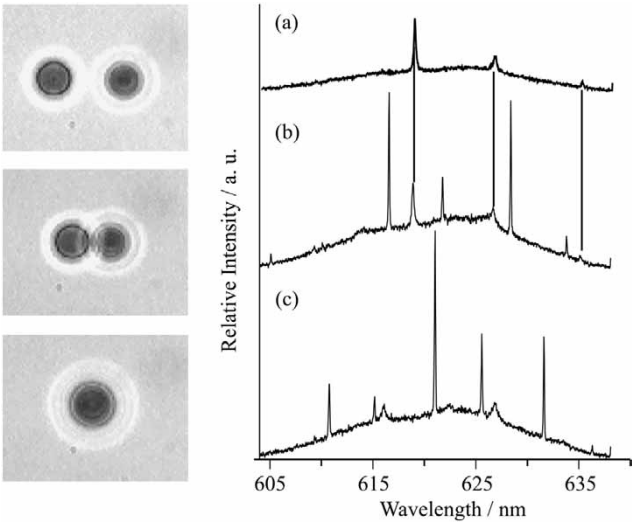

Figure 38. Illustration of the control that can be achieved over aerosol coagulation and the accompanying spectra of two water droplets, trapped with a laser operating at a wavelength of 514.5 nm. SRS fingerprints for: (a) right droplet in the image, (b) left and right droplets (combined volume $3.905 \times 10^{-16}\,m^3$) and (c) coagulated droplet (volume $3.902 \times 10^{-16}\,m^3$). [Ref. 62 – Reproduced by permission of the PCCP Owner Societies]

within an aqueous droplet, and the formation and behaviour of solid inclusions within a liquid host. Raman spectroscopy when combined with aerosol optical tweezers can provide a strategy for investigating these problems in detail [136].

As introduced in the preceding section, aerosol tweezers can be used to form multiple optical traps in parallel [140]. For example, two aqueous droplets can be trapped and manipulated independently, as illustrated in figure 38. By independent manipulation, the coagulation of the two droplets can be controlled. As an illustration of the accuracy with which the size of droplets can be determined from the wavelengths of the WGMs, we can compare the combined volume of the two droplets prior to coagulation with the single droplet volume following coagulation. The WGMs arising from the two droplets can be distinguished by independently moving the droplets in and out of the Raman active area and acquiring spectra of each (spectra a and b). When the combined volume is compared with the final volume determined from the spectrum of the coagulated droplet (spectrum c), the two are in agreement with an error of $<1 \times 10^{-18}\,m^3$ [62, 140].

A similar strategy can be adopted to characterize the coagulation and mixing state of aerosol droplets of different components [136]. For example, we have investigated the coagulation of a decane droplet with a water droplet. The approach is illustrated in figure 39. An aqueous droplet is trapped within one optical trap and an oil droplet within a second trap. The spectra can be recorded of each droplet independently before coagulation and mixing of the two aerosol components is performed. After coagulation, the spectrum of the multiphase coagulated droplet is recorded. The WGMs apparent in the spectra of the two pure droplets are lost on coagulation. Quenching of the WGMs is attributed to the formation of an inhomogeneous mixed droplet in which the WGMs are disrupted by the presence of surface lenses of decane or water.

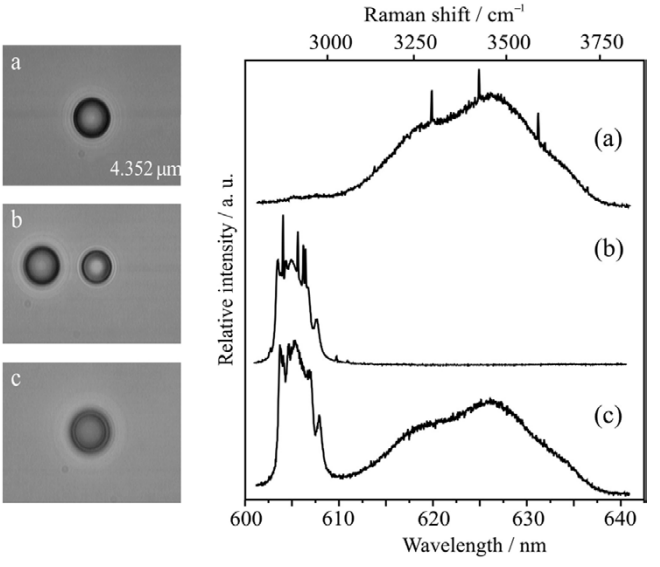

Figure 39. Images and spectra of the controlled coagulation of a decane droplet with a water droplet, trapped with a laser operating at a wavelength of 514.5 nm: (a) image and spectrum of the initially trapped water droplet of radius 4.352 μm; (b) image of the water (left) and decane (right) droplets, prior to coagulation, and spectrum of the decane droplet (the water droplet has been translated to the left of the image, out of the field of collection of the Raman scattered light); (c) the image and spectrum of the multicomponent water/decane droplet following controlled coagulation. [Reprinted with permission from ref. 136. Copyright 2006 American Chemical Society]

The two components are known to be immiscible in the bulk phase and immiscibility is also observed in the coagulated droplets. This can be confirmed by examining the shape of the OH stretching band. As described earlier, the OH band shape provides a signature of the hydrogen bonding environment of water molecules. In these coagulation experiments, the OH band shape of the coagulated droplet is consistent with the band shape of an aqueous droplet, demonstrating that the hydrogen bonding network has not been perturbed by the mixing of the two components. This is consistent with phase segregated organic and aqueous phases within the droplet.

The comparison of the controlled coagulation of two water droplets with the coagulation of a decane droplet with a water droplet provides a further illustration of the versatility of combining the spectroscopic methods for characterizing the aerosol with the optical tweezing approach for exercising precise control over single or multiple aerosol droplets.

6. Conclusions

The objective of this review has been to explore the spectroscopic characterization of liquid aerosol droplets directly and non-intrusively. We have considered the complementary information that may be obtained from both linear and non-linear

spectroscopic techniques, specifically spontaneous and stimulated Raman spectroscopy. The former allows the composition of the droplet to be probed and provides a signature that is consistent with measurements in bulk samples. This can allow the interpretation of the shape of spectral bands, such as that arising from the excitation of the OH stretching in water, in the same way as in bulk phase measurements, allowing information on intermolecular interactions to be gained.

SRS arises when the intensity of spontaneous Raman scattering surpasses a threshold above which the inelastic scatter can grow exponentially. The existence of WGMs provides a mechanism for spontaneous Raman scatter to become trapped within the droplet, allowing the build up of Raman intensity and the threshold condition to be satisfied. Once again, the resulting SRS signature is shown to be consistent with both the spontaneous Raman signature from a bulk sample and from droplets. The non-linear origin of the signal leads to a spectral signature of chemical components that scales exponentially with species concentration, providing an extremely accurate probe of droplet composition. The threshold condition does, however, impose a severe limitation on the detection of trace components, and the resonance condition reduces the likelihood of detecting species with narrow Raman linewidths with decreasing droplet size. The SRS fingerprint of WGM wavelengths can allow the size of the droplet to be determined with nanometre accuracy providing a powerful technique for investigating aerosol processes that lead to changes in particle size.

The applications of these techniques in studies of droplet evaporation, equilibrium particle size and composition, and aerosol coagulation and mixing state have been highlighted. While the first example illustrates the advantages of non-linear spectroscopy for accurately determining droplet composition, the second illustrates the value in accurate determination of droplet size, allowing the fundamental factors that govern aerosol size distributions to be rigorously studied. The final example highlights the ability to probe inhomogeneities in composition within a single particle with the spectral signatures providing an opportunity to characterize the mixing state of different chemical components.

Through the combination of the spectroscopic techniques we have reviewed and the new techniques for the optical control and manipulation of aerosol particles, a new approach for characterizing aerosol particle dynamics has been established. It is anticipated that this approach will yield important new insights into the fundamental factors governing particle size, composition, mixing state and the factors that govern the physical and chemical transformation of aerosols.

Acknowledgements

LM thanks the EPSRC for financial support. The RSC and EPSRC are acknowledged for financial support for HM through the Analytical Trust Fund. Kate Hanford is acknowledged for her assistance in some of the measurements.

References

[1] *Analytical Chemistry of Aerosols*, edited by K. R. Spurny (CRC Press LLC, 1999).
[2] R. C. Flagan, Aerosol Sci. Tech. **28**(4), 301 (1998).

[3] M. Z. Martin, M. D. Cheng, and R. C. Martin, Aerosol Sci. Tech. **31**(6)**,** 409 (1999).
[4] T. A. Cahill and P. Wakabayashi, Advances in Chemistry Series **232,** 211 (1993).
[5] M. F. Sipin, S. A. Guazzotti, and K. A. Prather, Anal. Chem. **75**(12)**,** 2929 (2003).
[6] P. H. McMurry, Atmos. Environ. **34**(12–14)**,** 1959 (2000).
[7] B. J. Turpin, P. Saxena, and E. Andrews, Atmos. Environ. **34**(18)**,** 2983 (2000).
[8] J. C. Chow, J. Air Waste Manage. Assoc. **45,** 320 (1995).
[9] C. A. Noble and K. A. Prather, Mass Spec. Rev. **19**(4)**,** 248 (2000).
[10] S. N. Pandis, A. S. Wexler, and J. H. Seinfeld, J. Phys. Chem. **99,** 9646 (1995).
[11] J. H. Seinfeld and S. N. Pandis, *Atmospheric Chemistry and Physics: From Air Pollution to Climate Change* (John Wiley & Sons, New York, 1998).
[12] G. McFiggans, P. Artaxo, U. Baltensperger, H. Coe, M. C. Facchini, *et al*., Atmos. Chem. Phys. Disc. **5,** 8507 (2005).
[13] M. Y. Choi and C. K. Chan, J. Phys. Chem. A **109**(6)**,** 1042 (2005).
[14] I. N. Tang, A. C. Tridico, and K. H. Fung, J. Geophys. Res. **102**(D19)**,** 23269 (1997).
[15] C. A. Colberg, U. K. Krieger, and T. Peter, J. Phys. Chem. A **108**(14)**,** 2700 (2004).
[16] M. Kanakidou, J. H. Seinfeld, S. N. Pandis, I. Barnes, F. J. Dentener, *et al*., Atmos. Chem. and Phys. **5,** 1053 (2005).
[17] Y. Rudich, Chem. Rev. **103,** 5097 (2003).
[18] C. N. Cruz and S. N. Pandis, Environ. Sci. Tech. **34**(20)**,** 4313 (2000).
[19] A. J. Prenni, P. J. De Mott, and S. M. Kreidenweis, Atmos. Environ. **37**(30)**,** 4243 (2003).
[20] M. Y. Choi and C. K. Chan, Environ. Sci. Tech. **36**(11)**,** 2422 (2002).
[21] G. B. Ellison, A. F. Tuck, and V. Vaida, J. Geophys. Res. **104**(D9)**,** 11633 (1999).
[22] D. J. Donaldson, A. F. Tuck, and V. Vaida, Phys. Chem. Chem. Phys. **3**(23)**,** 5270 (2001).
[23] M. N. Chan and C. K. Chan, Atmos. Chem. and Phys. **5,** 2703 (2005).
[24] E. J. Davis and G. Schweiger, *The Airborne Microparticle* (Springer, New York, 2002).
[25] V. Devarakonda and A. K. Ray, J. Colloid Interface Sci. **221,** 104 (2000).
[26] R. J. Hopkins and J. P. Reid, J. Phys. Chem. B **110,** 3239 (2006).
[27] J. Smolik and J. Vitovec, J. Aerosol Sci. **15**(5)**,** 545 (1984).
[28] F. R. Newbold and N. R. Amundson, Aiche Journal **19**(5)**,** 1042 (1973).
[29] R. J. Hopkins, C. R. Howle, and J. P. Reid, Phys. Chem. Chem. Phys. **8,** 2879 (2006).
[30] P. H. Kaye, K. Alexander-Buckley, E. Hirst, and S. Saunders, J. Geophys. Res. **101,** 19215 (1996).
[31] P. H. Kaye, Meas. Sci. Tech. **9**(2)**,** 141 (1998).
[32] P. H. Kaye, J. E. Barton, E. Hirst, and J. M. Clark, Appl. Opt. **39**(21)**,** 3738 (2000).
[33] Z. Ulanowski, R. S. Greenaway, P. H. Kaye, and I. K. Ludlow, Meas. Sci. Tech. **13**(3)**,** 292 (2002).
[34] Z. Ulanowski, E. Hesse, P. H. Kaye, A. J. Baran, and R. Chandrasekhar, J. Quant. Spec. Radia. Trans. **79,** 1091 (2003).
[35] C. F. Bohren and D. R. Huffman, *Absorption and Scattering of Light by Small Particles* (John Wiley and Sons, New York, 1983).
[36] J. F. Widmann, C. L. Aardahl, and E. J. Davis, Trac–Trends in Anal. Chem. **17**(6)**,** 339 (1998).
[37] R. Symes, R. M. Sayer, and J. P. Reid, Phys. Chem. Chem. Phys. **6,** 474 (2004).
[38] G. Schweiger, J. Aerosol Sci. **21**(4)**,** 483 (1990).
[39] J. P. Reid and L. Mitchem, Annu. Rev. Phys. Chem. **57,** 245 (2006).
[40] E. J. Davis, Aerosol Sci. Tech. **26**(3)**,** 212 (1997).
[41] T. H. Lilley, in *Water: A Comprehensive Treatise*, edited by F. Franks (Plenum, New York, 1973) Vol. 3, p. 265.
[42] G. E. Walrafen, in *Water: A Comprehensive Treatise*, edited by F. Franks (Plenum, New York, 1972) Vol. 1, p. 151.
[43] J. R. Scherer, M. K. Go, and S. Kint, J. Phys. Chem. **78**(13)**,** 1304 (1974).
[44] J. D. Smith, C. D. Cappa, K. R. Wilson, R. C. Cohen, P. L. Geissler, *et al*., Proc. Nat. Acad. Sci. USA **102**(40)**,** 14171 (2005).
[45] P. Terpstra, D. Combes, and A. Zwick, J. Chem. Phys. **92,** 65 (1990).
[46] D. E. Hare and C. M. Sorensen, J. Chem. Phys. **93**(1)**,** 25 (1990).
[47] K. Cunningham and P. A. Lyons, J. Chem. Phys. **59**(4)**,** 2132 (1973).
[48] G. Darrigo, G. Maisano, F. Mallamace, P. Migliardo, and F. Wanderlingh, J. Chem. Phys. **75**(9)**,** 4264 (1981).
[49] G. E. Walrafen, M. R. Fisher, M. S. Hokmabadi, and W. H. Yang, J. Chem. Phys. **85**(12)**,** 6970 (1986).
[50] R. H. Li, Z. P. Jiang, F. G. Chen, H. W. Yang, and Y. T. Guan, J. Mol. Str. **707**(1–3)**,** 83 (2004).
[51] R. J. Hopkins and J. P. Reid, J. Phys. Chem. A **109,** 7923 (2005).
[52] R. J. Hopkins, R. Symes, R. M. Sayer, and J. P. Reid, Chem. Phys. Lett. **380,** 665 (2003).
[53] S. C. Hill and R. E. Benner, in *Optical Effects Associated with Small Particles*, edited by P. W. Barber and R. K. Chang (World Scientific, Singapore, 1988) Vol. 1, p. 3.

[54] J. Popp, M. Lankers, M. Trunk, I. Hartmann, E. Urlaub, *et al*., Appl. Spec. **52**(2)**,** 284 (1998).
[55] A. J. Campillo, J. D. Eversole, and H. B. Lin, in *Optical Processes in Microcavities*, edited by R. K. Chang and A. J. Campillo (World Scientific, Singapore, 1996).
[56] A. Biswas, H. Latifi, R. L. Armstrong, and R. G. Pinnick, Phys. Rev. A **40**(12)**,** 7413 (1989).
[57] R. Thurn and W. Kiefer, Appl. Opt. **24**(10)**,** 1515 (1985).
[58] J. D. Eversole, H. B. Lin, A. L. Huston, A. J. Campillo, P. T. Leung, *et al*., J. Opt. Soc. Am. B **10**(10)**,** 1955 (1993).
[59] M. Y. Choi, C. K. Chan, and Y. H. Zhang, J. Phys. Chem. A **108**(7)**,** 1133 (2004).
[60] R. M. Sayer, R. D. B. Gatherer, and J. P. Reid, Phys. Chem. Chem. Phys. **5**(17)**,** 3740 (2003).
[61] R. N. Berglund and B. Y. H. Liu, Environ. Sci. Technol. **7,** 147 (1973).
[62] R. J. Hopkins, L. Mitchem, A. D. Ward, and J. P. Reid, Phys. Chem. Chem. Phys. **6**(21)**,** 4924 (2004).
[63] L. Mitchem, J. Buajarern, R. J. Hopkins, A. D. Ward, R. J. J. Gilham, *et al*., J. Phys. Chem. A **110,** 8116 (2006).
[64] A. Ashkin, J. M. Dziedzic, J. E. Bjorkholm, and S. Chu, Opt. Lett. **11**(5)**,** 288 (1986).
[65] J. E. Molloy and M. J. Padgett, Contemp. Phys. **43**(4)**,** 241 (2002).
[66] W. Singer, S. Bernet, N. Hecker, and M. Ritsch-Marte, J. Mod. Opt. **47**(14–15)**,** 2921 (2000).
[67] P. Wernet, D. Nordlund, U. Bergmann, M. Cavalleri, M. Odelius, *et al*., Science **304**(5673)**,** 995 (2004).
[68] J. Stenger, D. Madsen, P. Hamm, E. T. J. Nibbering, and T. Elsaesser, Phys. Rev. Lett. **8702**(2) (2001).
[69] W. Sutherland, Phil. Mag. **50,** 460 (1900).
[70] J. D. Bernal and R. H. Fowler, J. Chem. Phys. **1**(8)**,** 515 (1933).
[71] M. Starzak and M. Mathlouthi, Food Chemistry **82**(1)**,** 3 (2003).
[72] J. D. Smith, C. D. Cappa, K. R. Wilson, B. M. Messer, R. C. Cohen, *et al*., Science **306**(5697)**,** 851 (2004).
[73] J. B. Brubach, A. Mermet, A. Filabozzi, A. Gerschel, and P. Roy, J. Chem. Phys. **122**(18) (2005).
[74] Z. H. Wang, A. Pakoulev, Y. Pang, and D. D. Dlott, Chem. Phys. Lett. **378**(3–4)**,** 281 (2003).
[75] K. H. Fung and I. N. Tang, Appl. Spec. **46**(7)**,** 1189 (1992).
[76] R. Vehring and G. Schweiger, Appl. Spectrosc. **46**(1)**,** 25 (1992).
[77] R. Vehring, C. L. Aardahl, G. Schweiger, and E. J. Davis, J. Aerosol Sci. **29**(9)**,** 1045 (1998).
[78] G. Schweiger, J. Opt. Soc. Am. B **8**(8)**,** 1770 (1991).
[79] K. H. Fung, D. G. Imre, and I. N. Tang, J. Aerosol Sci. **25**(3)**,** 479 (1994).
[80] G. E. B. Ahlijah and E. F. Mooney, Spectrochim. ActaA **25**(3)**,** 619 (1969).
[81] E. Spinner, Spectrochim. Acta **59**(7)**,** 1441 (2003).
[82] J. B. Snow, S. X. Qian, and R. K. Chang, Opt. Lett. **10**(1)**,** 37 (1985).
[83] H. B. Lin, J. D. Eversole, and A. J. Campillo, Opt. Comm. **77**(5–6)**,** 407 (1990).
[84] H. B. Lin, A. L. Huston, J. D. Eversole, and A. J. Campillo, J. Opt. Soc. Am. B **7**(10)**,** 2079 (1990).
[85] H. B. Lin, J. D. Eversole, and A. J. Campillo, Opt. Lett. **17**(11)**,** 828 (1992).
[86] J. Z. Zhang, D. H. Leach, and R. K. Chang, Opt. Lett. **13**(4)**,** 270 (1988).
[87] S. X. Qian, J. B. Snow, and R. K. Chang, Opt. Lett. **10**(10)**,** 499 (1985).
[88] F. H. Wirth, K. A. Juvan, D. H. Leach, J. C. Swindal, R. K. Chang, *et al*., Opt. Lett. **17**(19)**,** 1334 (1992).
[89] J. Z. Zhang and R. K. Chang, J. Opt. Soc. Am. B **6**(2)**,** 151 (1989).
[90] J. Z. Zhang, G. Chen, and R. K. Chang, J. Opt. Soc. Am. B **7**(1)**,** 108 (1990).
[91] H. M. Tzeng, K. F. Wall, M. B. Long, and R. K. Chang, Opt. Lett. **9**(11)**,** 499 (1984).
[92] S. X. Qian, J. B. Snow, H. M. Tzeng, and R. K. Chang, Science **231**(4737)**,** 486 (1986).
[93] D. H. Leach, R. K. Chang, W. P. Acker, and S. C. Hill, J. Opt. Soc. Am. B **10**(1)**,** 34 (1993).
[94] W. P. Acker, D. H. Leach, and R. K. Chang, Opt. Lett. **14**(8)**,** 402 (1989).
[95] P. Chylek, H. B. Lin, J. D. Eversole, and A. J. Campillo, Opt. Lett. **16**(22)**,** 1723 (1991).
[96] H. B. Lin, A. L. Huston, J. D. Eversole, B. L. Justus, and A. J. Campillo, J. Opt. Soc. Am. B **3**(8)**,** 250 (1986).
[97] H. B. Lin and A. J. Campillo, Opt. Lett. **20**(15)**,** 1589 (1995).
[98] J. D. Eversole, H. B. Lin, and A. J. Campillo, J. Opt. Soc. Am. B **12**(2)**,** 287 (1995).
[99] P. Chylek, J. Opt. Soc. Am. **66,** 285 (1976).
[100] J. R. Probert-Jones, J. Opt. Soc. Am. A **1,** 822 (1984).
[101] H. B. Lin, A. L. Huston, J. D. Eversole, A. J. Campillo, and P. Chylek, Opt. Lett. **17**(14)**,** 970 (1992).
[102] A. K. Ray, A. Souyri, E. J. Davis, and T. M. Allen, Appl. Opt. **30**(27)**,** 3974 (1991).
[103] R. M. Sayer, R. D. B. Gatherer, R. Gilham, and J. P. Reid, Phys. Chem. Chem. Phys. **5,** 3732 (2003).
[104] G. E. Walrafen, Adv. Mol. Relax. Proc. **3,** 43 (1972).
[105] G. E. Walrafen and M. J. Colles, Appl. Spec. **25**(1)**,** 142 (1971).
[106] M. G. Sceats, S. A. Rice, and J. E. Butler, J. Chem. Phys. **64**(6)**,** 2701 (1976).
[107] H. Yui, H. Fujiwara, and T. Sawada, Chem. Phys. Lett. **360**(1–2)**,** 53 (2002).
[108] H. Yui and T. Sawada, Phys. Rev. Lett. **85**(16)**,** 3512 (2000).
[109] R. Symes, R. J. J. Gilham, R. M. Sayer, and J. P. Reid, Phys. Chem. Chem. Phys. **7**(7)**,** 1414 (2005).

[110] J. G. Xie, T. E. Ruekgauer, J. Gu, R. L. Armstrong, and R. G. Pinnick, Appl. Opt. **33**(3)**,** 368 (1994).
[111] R. Vehring, J. Aerosol Sci. **29**(1–2)**,** 65 (1998).
[112] H. B. Lin and A. J. Campillo, Phys. Rev. Lett. **73**(18)**,** 2440 (1994).
[113] S. C. Ching, H. M. Lai, and K. Young, J. Opt. Soc. Am. B **4**(12)**,** 1995 (1987).
[114] S. C. Ching, H. M. Lai, and K. Young, J. Opt. Soc. Am. B **4**(12)**,** 2004 (1987).
[115] H. Yokoyama and S. D. Brorson, J. Appl. Phys. **66,** 4801 (1989).
[116] R. W. Boyd, *Nonlinear Optics* (Academic Press, New York, 1992).
[117] A. J. Campillo, J. D. Eversole, and H. B. Lin, J. Chem. Phys. **109**(20)**,** 9199 (1998).
[118] J. X. Zhang, P. A. Moortgat, and P. M. Aker, J. Chem. Phys. **105**(17)**,** 7276 (1996).
[119] S. R. Dillon and R. C. Dougherty, J. Phys. Chem. A **106**(34)**,** 7647 (2002).
[120] J. S. Huang, C. B. Ke, L. S. Huang, and K. C. Lin, Spectrochim. Acta B **57**(1)**,** 35 (2002).
[121] C. Favre, V. Boutou, S. C. Hill, W. Zimmer, M. Krenz, *et al*., Phys. Rev. Lett. **89**(3), art. no (2002).
[122] J. H. Eickmans, S. X. Qian, and R. K. Chang, Particle Characterization **4**(3)**,** 85 (1987).
[123] A. Serpenguzel, G. Chen, and R. K. Chang, Part. Sci. Tech. **8,** 179 (1990).
[124] V. E. Roman, J. Popp, M. H. Fields, and W. Kiefer, J. Opt. Soc. Am. B **16**(3)**,** 370 (1999).
[125] V. E. Roman, J. Popp, M. H. Fields, and W. Kiefer, Appl. Opt. **38**(9)**,** 1418 (1999).
[126] M. M. Mazumder, K. Schaschek, R. K. Chang, and J. B. Gillespie, Chem. Phys. Lett. **239**(4–6)**,** 361 (1995).
[127] R. Symes, H. Meresman, R. M. Sayer, and J. P. Reid, Chem. Phys. Lett. **419,** 545 (2006).
[128] M. H. Fields, J. Popp, and R. K. Chang, Opt. Lett. **21**(18)**,** 1457 (1996).
[129] A. S. Kwok and R. K. Chang, Opt. Lett. **17**(18)**,** 1262 (1992).
[130] L. Pasternack, J. W. Fleming, and J. C. Owrutsky, J. Opt. Soc. Am. B **13**(7)**,** 1510 (1996).
[131] R. Symes and J. P. Reid, Phys. Chem. Chem. Phys. **8,** 293 (2006).
[132] W. F. Hsieh, J. B. Zheng, and R. K. Chang, Opt. Lett. **13**(6)**,** 497 (1988).
[133] A. Serpenguzel, G. Chen, R. K. Chang, and W. F. Hsieh, J. Opt. Soc. Am. B **9**(6)**,** 871 (1992).
[134] S. X. Qian, S. Yuan, Y. Li, H. Wang, X. Huang, *et al*., Opt. Communs. **74,** 414 (1990).
[135] A. Biswas, R. L. Armstrong, and R. G. Pinnick, Opt. Lett. **15**(21)**,** 1191 (1990).
[136] L. Mitchem, J. Buajarern, A. D. Ward, and J. P. Reid, J. Phys. Chem. B **110,** 13700 (2006).
[137] R. Chang and E. J. Davis, J. Col. Inter. Sci. **47**(1)**,** 65 (1974).
[138] A. K. Ray and S. Venkatraman, Aiche Journal **41**(4)**,** 938 (1995).
[139] L. Mitchem, R. J. Hopkins, J. Buajarern, A. D. Ward, and J. P. Reid, Chem. Phys. Lett. **432,** 362 (2006).
[140] J. Buajarern, L. Mitchem, A. D. Ward, N. H. Nahler, D. McGloin, and J. P. Reid, J. Chem. Phys. **125,** 114506 (2006).